Multi-Carrier Agile Phased Array Radar

Tianyao Huang, Nir Shlezinger, *Member, IEEE*, Xingyu Xu, Dingyou Ma,
Yimin Liu, *Member, IEEE*, and Yonina C. Eldar, *Fellow, IEEE*

***Abstract*—Modern radar systems are expected to operate reliably in congested environments. A candidate technology for meeting these demands is frequency agile radar (FAR), which randomly changes its carrier frequencies. FAR is known to improve the electronic counter-countermeasures (ECCM) performance while facilitating operation in congested setups. To enhance the target recovery performance of FAR in complex electromagnetic environments, we propose two radar schemes extending FAR to multi-carrier waveforms. The first is Wideband Multi-carrier Agile Radar (WMAR), which transmits/receives wideband waveforms simultaneously with every antenna. To mitigate the demanding hardware requirements associated with wideband waveforms used by WMAR, we next propose multi-Carrier AgilE phaSed Array Radar (CAESAR). CAESAR uses narrowband monotone waveforms, thus facilitating ease of implementation of the system, while introducing *spatial agility*. We characterize the transmitted and received signals of the proposed schemes, and develop an algorithm for recovering the targets, based on concepts from compressed sensing to estimate the range-Doppler parameters of the targets. We then derive conditions which guarantee their accurate reconstruction. Our numerical study demonstrates that both multi-carrier schemes improve performance compared to FAR while maintaining its practical benefits. We also demonstrate that the performance of CAESAR, which uses monotone waveforms, is within a small gap from the wideband radar.**

***Index Terms*—Frequency agile radar, compressed sensing, multi-carrier agility.**

I. Introduction

MODERN radars must be reliable, but at the same time compact, flexible, robust, and efficient in terms of cost and power usage [4]–[6]. A possible approach to meet these requirements is by exploiting *frequency agility* [4], namely, to utilize narrowband waveforms, while allowing the carrier frequencies to vary between different radar pulses. Among the main advantages of frequency agile radar (FAR) are its excellent electronic counter-countermeasures (ECCM) and electromagnetic compatibility (EMC) performance [4], and the fact that it has the flexibility of supporting spectrum sharing [6]. Finally, by utilizing narrowband signals with varying frequencies, FAR systems can synthesize a large bandwidth with narrowband waveforms [5], which simplifies the implementation.

A major drawback of FAR compared to wideband radar is its reduced range-Doppler reconstruction performance of targets. This reduced performance is a byproduct of the relatively small number of radar measurements processed by FAR, which stems from its usage of a single narrowband waveform for each pulse. The performance reduction can be relieved by using compressed sensing (CS) algorithms that exploit sparsity of the target scheme [7]. However, the degradation becomes notable in extremely congested or contested electromagnetic environments [1], where there may be no vacant bands in some pulses or some radar returns of the transmitted pulses may be discarded due to strong interference [8].

The performance degradation of FAR can be mitigated by using multi-carrier transmissions. When multiple carriers are transmitted simultaneously in a single pulse, the number of radar measurements is increased, and the target reconstruction performance is improved. Various multi-carrier radar schemes have been studied in the literature, including frequency division multiple access multiple-input multiple-output (FDMA-MIMO) [9], [10], sub-Nyquist multiple-input multiple-output radar (SUMMeR) [11], and frequency diversity array (FDA) radar [12], [13]. In the aforementioned schemes, different array elements transmit waveforms at different frequencies, usually forming an omnidirectional beam and illuminating a large field-of-view [14]. This degrades radar performance, especially in track mode, where a directional beam focusing on the target is preferred [14]. In addition, frequency agility is not exploited in FDMA-MIMO and FDA. The derivation of frequency agile multi-carrier schemes for phased array radar, leading to a focused beam with high gain, is the focus of this work.

Here, we propose two multi-carrier agile phased array radar schemes. The first uses all the antenna elements to transmit a single waveform consisting of multiple carriers simultaneously in each pulse. Frequency agility is induced by randomly selecting the carriers utilized, resulting in a wideband multi-carrier agile radar (WMAR) scheme. While the increased number of carriers is shown to achieve improved reconstruction performance compared to FAR [1], WMAR utilizes multiband signals of large instantaneous bandwidth. Therefore, its implementation does not benefit from the simplifications associated with utilizing conventional narrowband monotone signals, and may suffer from envelope fluctuation [15].

Manuscript received May 9, 2020; revised September 14, 2020; accepted September 15, 2020. Date of publication September 24, 2020; date of current version October 12, 2020. The associate editor coordinating the review of this manuscript and approving it for publication was Dr. Athanasios A. Rontogiannis. This work was supported by the National Natural Science Foundation of China under Grants 61801258 and 61571260, in part by the European Unions Horizon 2020 research and innovation program under Grant 646804-ERC-COG-BNYQ, and in part by the Air Force Office of Scientific Research under Grant FA9550-18-1-0208. Parts of this work were presented in previous conferences [1]–[3]. *(Corresponding author: Yimin Liu.)*

Tianyao Huang, Xingyu Xu, Dingyou Ma, and Yimin Liu are with the Department of Electronic Engineering, Tsinghua University, Beijing 100084, China (e-mail: huangtianyao2009@gmail.com; xy-xu19@mails.tsinghua.edu.cn; mdy16@mails.tsinghua.edu.cn; yiminliu@tsinghua.edu.cn).

Nir Shlezinger is with the School of ECE, Ben-Gurion University of the Negev, Be'er-Sheva 84105, Israel (e-mail: nirshlezinger1@gmail.com).

Yonina C. Eldar is with the Faculty of Math and CS, Weizmann Institute of Science, Rehovot 7610001, Israel (e-mail: yonina.eldar@weizmann.ac.il).

Digital Object Identifier 10.1109/TSP.2020.3026186

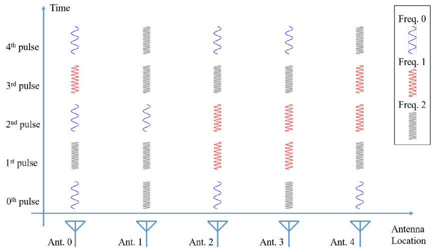

Fig. 1. Transmission example of CAESAR. In every pulse of this example, two out of three carrier frequencies are emitted by different sub-arrays. For example, frequency 0 and 2 are selected in the 0-th pulse and are sent by antenna 0, 2, 4, and antenna 1, 3, respectively. FAR or FDMA-MIMO/FDA can be regarded as a special case of CAESAR, with only one out of three frequencies or all available frequencies sent in each pulse.

To overcome the use of instantaneously wideband waveforms, we next develop multi-Carrier AgilE phaSed Array Radar (CAESAR), which combines frequency agility and *spatial agility*. Specifically, CAESAR selects a small number of carrier frequencies on each pulse and randomly allocates different carrier frequencies among its antenna elements, such that each array element transmits a narrowband constant modulus waveform, facilitating system implementation. An illustration of this transmission scheme is depicted in Fig. 1.

For each carrier frequency, dedicated phase shifts on the corresponding sub-array elements are used to yield a directional transmit beam, allowing to illuminate the tracked target in a similar manner as phased array radar. Despite the fact that only a sub-array antenna is utilized for each frequency, the antenna-frequency hopping strategy of CAESAR results in array antenna gain loss and a relatively small performance gap compared to wideband radar equipped with the same antenna array. Furthermore, the combined randomization of frequency and antenna allocation can be exploited to realize a dual function radar-communications (DFRC) system [16] by embedding digital information into the selection of these parameters. We study the application of CAESAR as a DFRC system in a companion paper [17], and focus here on the radar and its performance.

To present WMAR and CAESAR, we characterize the signal model for each approach, based on which we develop a recovery algorithm for high range resolution (HRR), Doppler, and angle estimation of radar targets. Our proposed algorithm utilizes CS methods for range-Doppler reconstruction, exploiting its underlying sparsity, and applies matched filtering to detect the angles of the targets. We provide a detailed theoretical analysis of the range-Doppler recovery performance of our proposed algorithm under complex electromagnetic environments. In particular, we prove that CAESAR and WMAR are guaranteed to recover with high probability a number of scattering points which grows proportionally to the square root of the number of different narrowband signals used, i.e., the number of carrier frequencies that are simultaneously transmitted in each pulse. This theoretical result verifies that increasing the number of carriers improves target recovery, and reduces performance degradation due to intense interference in complex electromagnetic environments. WMAR and CAESAR are evaluated in a numerical study, where it is shown that their range-Doppler reconstruction performance as well as robustness to interference are substantially improved compared to FAR. Additionally, it is demonstrated that the performance of CAESAR is only within a small gap from that achievable using wideband WMAR. Our previous conference papers [1], [2] introduced the preliminary conceptual ideas behind WMAR and CAESAR, while [3] outlined their theoretical analysis. The current journal paper presents a comprehensive unified description of WMAR and CAESAR as multi-carrier agile phased array radar schemes, as well as provides comparison with related schemes, complete theoretical analysis with detailed proofs, and extensive simulation study.

The remainder of the article is structured as follows: Sections II and III present WMAR and CAESAR, respectively. Section IV introduces the recovery algorithm to estimate the range, Doppler, and angle of the targets. In Section V we discuss the pros and cons of each scheme compared to related radar methods. Section VI derives theoretical performance measures of the recovery method. Simulation results are presented in Section VII, and Section VIII concludes the article.

Throughout the article, we use $\mathbb{C}$, $\mathbb{R}$ to denote the sets of complex, real numbers, respectively, and use $|\cdot|$ for the magnitude or cardinality of a scalar number, or a set, respectively. Given $x \in \mathbb{R}$, $\lfloor x \rfloor$ denotes the largest integer less than or equal to x, and $\binom{n}{k} = \frac{n!}{k!(n-k)!}$ represents the binomial coefficient. Uppercase boldface letters denote matrices (e.g., $\boldsymbol{A}$), and boldface lowercase letters denote vectors (e.g., $\boldsymbol{a}$). The (n, m)-th element of a matrix $\boldsymbol{A}$ is denoted as $[\boldsymbol{A}]_{m,n}$, and similarly $[\boldsymbol{a}]_n$ is the n-th entry of the vector $\boldsymbol{a}$. Given a matrix $\boldsymbol{A} \in \mathbb{C}^{M\times N}$, and a number n (or a set of integers, Λ), $[\boldsymbol{A}]_n$ ($[\boldsymbol{A}]_\Lambda \in \mathbb{C}^{M\times|\Lambda|}$) is the n-th column of $\boldsymbol{A}$ (the sub-matrix consisting of the columns of $\boldsymbol{A}$ indexed by Λ). Similarly, $[\boldsymbol{a}]_\Lambda \in \mathbb{C}^{|\Lambda|}$ is the sub-vector consisting of the elements of $\boldsymbol{a} \in \mathbb{C}^N$ indexed by Λ. The complex conjugate, transpose, and the complex conjugate-transpose are denoted $(\cdot)^*$, $(\cdot)^T$, $(\cdot)^H$, respectively. We denote $\|\cdot\|_p$ as the ℓ_p norm, $\|\cdot\|_0$ is the number of non-zero entries, and $\|\cdot\|_F$ is the Frobenius norm. The probability measure is $\mathbb{P}(\cdot)$, while $\mathrm{E}[\cdot]$ and $\mathrm{D}[\cdot]$ are the expectation and variance of a random argument, respectively.

II. WMAR

In this section we present the proposed WMAR scheme, which originates from FAR [4], aiming to increase the number of radar measurements and improve the range-Doppler recovery performance. We first briefly review FAR in Subsection II-A. Then, we detail the proposed WMAR in Subsection II-B, and present the resulting radar signal model in Subsection II-C.

A. Preliminaries of FAR

FAR [4] is a technique for enhancing the ECCM and EMC performance of radar systems by using randomized carrier frequencies. In the following we consider a radar system equipped with L antenna elements, uniformly located on an antenna array with distance d between two adjacent elements. Let N be the number of radar pulses transmitted in each coherent processing interval (CPI). Radar pulses are repeatedly transmitted, starting from time instance nT_r to $nT_r + T_p$, $n \in \mathcal{N} := \{0, 1, \dots, N-1\}$, where T_r and T_p represent the pulse repetition interval and pulse duration, respectively, and $T_r > T_p$. Let $\mathcal{F}$ be the set of available carrier frequencies, given by $\mathcal{F} := \{f_c + m\Delta f | m \in \mathcal{M}\}$, where f_c is the initial carrier frequency, $\mathcal{M} := \{0, 1, \dots, M-$

$1\}$, M is the number of available frequencies, and Δf is the frequency step.

In the n-th radar pulse, FAR randomly selects a carrier frequency f_n from $\mathcal{F}$. The waveform sent from each antenna for the n-th pulse at time instance t is $\phi(f_n, t - nT_r)$, where

$$\phi(f,t) := \mathrm{rect}\left(t/T_p\right) e^{j2\pi f t}, \tag{1}$$

and $\mathrm{rect}(t) = 1$ for $t \in [0,1)$ and zero otherwise, representing rectangular envelope baseband signals.

In order to direct the antenna beam pointing towards a desired angle θ, the signal transmitted by each antenna is weighted by a phase shift $w_l(\theta, f_n) \in \mathbb{C}$ [18], given by

$$w_l(\theta, f) := e^{j2\pi f l d \sin\theta / c}, \tag{2}$$

where c denotes the speed of light. Define the vector $\boldsymbol{w}(\theta, f) \in \mathbb{C}^L$ whose l-th entry is $[\boldsymbol{w}(\theta,f)]_l := w_l(\theta, f)$. The transmitted signal can be written as

$$\boldsymbol{x}_{\mathrm{F}}(n,t) := \boldsymbol{w}(\theta, f_n)\phi(f_n, t - nT_r). \tag{3}$$

The vector $\boldsymbol{x}_{\mathrm{F}}(n,t) \in \mathbb{C}^L$ in (3) denotes the transmission vector of the full array for the n-th pulse at time instance t.

The fact that FAR transmits monotone waveform facilitates its realization. Furthermore, the frequency agility achieved by randomizing the frequencies between pulses enhances survivability in complex electromagnetic environments. However, this comes at the cost of reduced number of radar measurements, which degrades the target recovery performance, particularly in the presence of interference, where some of the radar returns are missed [1]. To overcome these drawbacks, in the following we propose WMAR, which extends FAR to multi-carrier transmissions.

B. WMAR Transmit Signal Model

WMAR extends FAR to multi-carrier signalling. Broadly speaking, WMAR transmits a single multiband waveform from all its antennas, maintaining frequency agility by randomizing a *subset* of the available frequencies on each pulse.

Specifically, in the n-th radar pulse, WMAR randomly selects a set of carrier frequencies $\mathcal{F}_n$ from $\mathcal{F}$, $\mathcal{F}_n \subset \mathcal{F}$. We assume that the cardinality of $\mathcal{F}_n$ is constant, i.e., $|\mathcal{F}_n| = K$ for each $n \in \mathcal{N}$, and write the elements of this set as $\mathcal{F}_n = \{\Omega_{n,k} | k \in \mathcal{K}\}$, $\mathcal{K} := \{0, 1, \ldots, K-1\}$. The portion of the n-th pulse of WMAR in the k-th frequency is given by $\boldsymbol{x}_{\mathrm{W},k}(n,t) := \frac{1}{\sqrt{K}}\boldsymbol{w}(\theta, \Omega_{n,k})\phi(\Omega_{n,k}, t - nT_r)$, and the overall transmitted vector is $\boldsymbol{x}_{\mathrm{W}}(n,t) = \sum_{k=1}^{K} \boldsymbol{x}_{\mathrm{W},k}(n,t)$, i.e.,

$$\boldsymbol{x}_{\mathrm{W}}(n,t) = \sum_{k=1}^{K} \frac{1}{\sqrt{K}} \boldsymbol{w}\left(\theta, \Omega_{n,k}\right) \phi\left(\Omega_{n,k}, t - nT_r\right), \tag{4}$$

where the factor $\frac{1}{\sqrt{K}}$ guarantees that (4) has the same total power as the FAR signal (3).

FAR is a special case of WMAR under the setting $K = 1$. By using multiple carriers simultaneously via wideband signalling, i.e., $K > 1$, WMAR transmits a highly directional beam, while improving the robustness to missed pulses compared to FAR. The improved performance stems from the use of multi-carrier transmission, which increases the number of radar measurements. To see this, we detail the received signal model of WMAR in the following subsection.

C. WMAR Received Signal Model

We next model the received signal processed by WMAR. To that aim, we focus on the time interval after the n-th pulse is transmitted, i.e., $nT_r + T_p < t < (n+1)T_r$. In this period, the radar receives echoes of the pulse, which are sampled and processed in discrete-time.

To formulate the radar returns, we assume an ideal scattering point, representing either target or clutter, with scattering coefficient $\beta \in \mathbb{C}$ located in the transmit beam of the radar with direction angle ϑ, i.e., $\vartheta \approx \theta$. Denote by $r(t)$ the range between the target/clutter and the first radar antenna array element at time t. The scattering point is moving at a constant velocity v radially along with the radar line of sight, i.e., $r(t) = r(0) + vt$. Under the "stop and hop" assumption [19, Ch. 2], which assumes that the target hops to a new location when the radar transmits a pulse and stays there until another pulse is emitted, the range in the n-pulse is approximated as

$$r(t) \approx r(nT_r) = r(0) + v \cdot nT_r, \quad nT_r < t < (n+1)T_r. \tag{5}$$

To model the received signal, we first consider the n-th radar pulse that reaches the target, denoted by $\tilde{x}(n,t)$. Let $\tilde{x}_k(n,t)$ be its component at frequency $\Omega_{n,k}$, i.e., $\tilde{x}(n,t) := \sum_{k=0}^{K-1} \tilde{x}_k(n,t)$. Note that $\tilde{x}_k(n,t)$ is a summation of delayed transmissions from the corresponding antenna elements. The delay for the l-th array element is $r(nT_r)/c + ld\sin\vartheta/c$. Under the narrowband, far-field assumption, using (2), we have that

$$\begin{aligned} \tilde{x}_k(n,t) &= \sum_{l=0}^{L-1} \left[\boldsymbol{x}_{\mathrm{W},k}(n, t - r(nT_r)/c)\right]_l e^{-j2\pi\Omega_{n,k} l d \sin\vartheta / c} \\ &= \boldsymbol{w}^H\left(\vartheta, \Omega_{n,k}\right) \boldsymbol{x}_{\mathrm{W},k}(n, t - r(nT_r)/c). \end{aligned} \tag{6}$$

Substituting (5) and the definition of $\boldsymbol{x}_{\mathrm{W},k}(n,t)$ into (6) yields

$$\tilde{x}_k(n,t) = \frac{\rho_{\mathrm{W}}(n,k,\delta_\vartheta)}{\sqrt{K}} \phi\left(\Omega_{n,k}, t - nT_r - \frac{r(0) + nvT_r}{c}\right), \tag{7}$$

where $\delta_\vartheta := \sin\vartheta - \sin\theta$ is the relative direction sine with respect to the transmit beam, and $\rho_{\mathrm{W}}(n,k,\delta_\vartheta) := \boldsymbol{w}^H(\vartheta, \Omega_{n,k})\boldsymbol{w}(\theta, \Omega_{n,k})$ is the transmit gain, expressed as

$$\rho_{\mathrm{W}}(n,k,\delta_\vartheta) = \sum_{l=0}^{L-1} e^{-j2\pi\Omega_{n,k} l d \delta_\vartheta / c}. \tag{8}$$

Note that $\rho_{\mathrm{W}}(n,k,\delta_\vartheta)$ approaches L when $\delta_\vartheta \approx 0$.

Having modeled the signal which reaches the target, we now derive the radar returns observed by the antenna array. After being reflected by the scattering point, the signal at the k-th frequency propagates back to the l-th radar array element with an extra delay of $r(nT_r)/c + ld\sin\vartheta/c$, resulting in

$$\left[\widetilde{\boldsymbol{y}}_{\mathrm{W},k}(n,t)\right]_l := \beta \tilde{x}_k\left(n, t - r(nT_r)/c - ld\sin\vartheta/c\right). \tag{9}$$

The echoes vector $\widetilde{\boldsymbol{y}}_{\mathrm{W},k}(n,t) \in \mathbb{C}^L$ can be written as

$$\begin{aligned} \widetilde{\boldsymbol{y}}_{\mathrm{W},k}(n,t) &= \beta \boldsymbol{w}^*\left(\vartheta, \Omega_{n,k}\right) \tilde{x}_k\left(n, t - r(nT_r)/c\right) \\ &\overset{(a)}{=} \frac{\beta}{\sqrt{K}} \boldsymbol{w}^*\left(\vartheta, \Omega_{n,k}\right) \rho_{\mathrm{W}}(n,k,\delta_\vartheta) \\ &\quad \times \phi\left(\Omega_{n,k}, t - nT_r - (2r(0) + 2nvT_r)/c\right), \end{aligned} \tag{10}$$

where (a) follows from (7).

The received echoes at all K frequencies are then separated and sampled independently by each array element. The signal $\widetilde{\boldsymbol{y}}_{\mathrm{W},k}(n,t)$ is sampled with a rate of $f_s = 1/T_p$ at time instants $t = nT_r + i/f_s$, $i = 0, 1, \ldots, \lfloor T_r f_s \rfloor - 1$, such that each pulse is sampled once. Every sample time instant corresponds to a coarse range cell (CRC), $r \in (\frac{i-1}{2f_s}c, \frac{i}{2f_s}c)$. The division to CRCs indicates coarse range information of scattering points. We focus on an arbitrary i-th CRC, assuming that the scattering point does not move between CRCs during a CPI, i.e., there exists some integer i such that $\frac{i-1}{2f_s}c < r(0) < \frac{i}{2f_s}c$ and $\frac{i-1}{2f_s}c < r(0) + vnT_r < \frac{i}{2f_s}c, n \in \mathcal{N}$.

Collecting radar returns from N pulses and L elements at the same CRC yields a data cube $\boldsymbol{Y}_{\rm W} \in \mathbb{C}^{L\times N\times K}$ with entries

$$[\boldsymbol{Y}_{\rm W}]_{l,n,k} := \left[\widetilde{\boldsymbol{y}}_{{\rm W},k}(n, nT_r + i/f_s)\right]_l, \tag{11}$$

where i is the CRC index. The data cube $\boldsymbol{Y}_{\rm W}$ is processed to estimate the refined range information, Doppler, and angle of the scattering point. Data cubes from different CRCs are processed identically and separately.

Finally, we formulate how the unknown parameters of the targets are embedded in the processed data cube $\boldsymbol{Y}_{\rm W}$. To that aim, define $\delta_r := r(0) - ic/2f_s$ as the high-range resolution distance, $c_{n,k} := (\Omega_{n,k} - f_c)/\Delta f \in \mathcal{M}$ as the carrier frequency index, and $\zeta_{n,k} = \Omega_{n,k}/f_c$ as the relative frequency factor. Then, denoting by $\tilde{\beta} := \beta e^{-j4\pi f_c \delta_r/c}$, $\tilde{r} := -4\pi\Delta f \delta_r/c$ and $\tilde{v} := -4\pi f_c v T_r/c$ the generalized scattering intensity, and the normalized range and velocity, respectively, and substituting (10) into (11), we have that

$$[\boldsymbol{Y}_{\rm W}]_{l,n,k} = \frac{\tilde{\beta} e^{j\tilde{r}c_{n,k}}}{\sqrt{K}} e^{j\tilde{v}n\zeta_{n,k}} e^{-j2\pi\frac{\Omega_{n,k} l d \sin\vartheta}{c}} \rho_{\rm W}(n,k,\delta_\vartheta). \tag{12}$$

The unknown parameters in (12) are $\tilde{\beta}$, $\tilde{r}$, $\tilde{v}$ and $(\sin\vartheta, \delta_\vartheta)$, which are used to reveal the scattering intensity $|\beta|$, HRR range $r(0)$, velocity v and angle ϑ of the target.

The above model can be naturally extended to noisy multiple scatterers. When there are S scattering points inside the CRC instead of a single one as assumed previously, the received signal is a summation of returns from all these points corrupted by additive noise, denoted by $\boldsymbol{N} \in \mathbb{C}^{L\times N\times K}$. Following (12), the entries of the data matrix are

$$[\boldsymbol{Y}_{\rm W}]_{l,n,k} = \frac{1}{\sqrt{K}} \sum_{s=0}^{S-1} \tilde{\beta}_s e^{j\tilde{r}_s c_{n,k}} e^{j\tilde{v}_s n\zeta_{n,k}} e^{-j2\pi\Omega_{n,k} l d \sin\vartheta_s/c} \times \rho_{\rm W}(n,k,\delta_{\vartheta_s}) + [\boldsymbol{N}]_{l,n,k}, \tag{13}$$

where $\{\tilde{\beta}_s\}$, $\{\tilde{r}_s\}$, $\{\tilde{v}_s\}$ and $\{\vartheta_s\}$ represent the sets of factors of scattering coefficients, ranges, velocities, and angles of the S scattering points, respectively, which are unknown and should be estimated. A method for recovering these parameters from the data cube $\boldsymbol{Y}_{\rm W}$ is detailed in Section IV.

WMAR has several notable advantages: First, as an extension of FAR, it preserves its frequency agility and is suitable for implementation with phased array antennas. Furthermore, as we discuss in Section V, its number of radar measurements for each CRC is increased by a factor of K compared to FAR, thus yielding increased robustness to interference. However, WMAR transmitters simultaneously send multiple carriers instead of a monotone as in FAR, which requires large instantaneous bandwidth, leading to envelope fluctuation and low amplifier efficiency. To overcome these issues, we introduce CAESAR in the following section, which utilizes narrowband radar transceivers while introducing spatial agility, enabling multi-carrier transmission using monotone signals at a cost of a minimal array antenna gain loss.

III. CAESAR

CAESAR, similarly to WMAR, extends FAR to multi-carrier transmission. However, unlike WMAR, CAESAR utilizes monotone signalling and reception, and is thus more suitable for implementation. We detail the transmit and receive models of CAESAR in Sections III-A and III-B, respectively.

A. CAESAR Transmit Signal Model

Broadly speaking, CAESAR extends FAR to multi-carrier signalling by transmitting monotone waveforms with varying frequencies from different antenna elements. The selection of the frequencies, as well as their allocation among the antenna elements, is randomized anew in each pulse, thus inducing both *frequency and spatial agility*.

To formulate CAESAR, we consider the same pulse radar formulation detailed in Section II. Similarly to WMAR detailed in Subsection II-B, in the n-th radar pulse, CAESAR randomly selects a set of carrier frequencies $\mathcal{F}_n = \{\Omega_{n,k} | k \in \mathcal{K}\}$ from $\mathcal{F}$. While WMAR uses the set of selected frequencies to generate wideband waveforms, CAESAR allocates a sub-array for each frequency, such that all the antenna array elements are utilized for transmission, each at a single carrier frequency. Denote by $f_{n,l} \in \mathcal{F}_n$ the frequency used by the l-th antenna array element, $l \in \mathcal{L} := \{0, 1, \ldots, L-1\}$. After phase shifting the waveform to direct the beam, the l-th array element transmission can be written as

$$[\boldsymbol{x}_{\rm C}(n,t)]_l := [\boldsymbol{w}(\theta, f_{n,l})]_l \, \phi(f_{n,l}, t - nT_r). \tag{14}$$

The vector $\boldsymbol{x}_{\rm C}(n,t) \in \mathbb{C}^L$ in (14) denotes the full array transmission vector for the n-th pulse at time t. Here, unlike FAR which transmits a single frequency from the full array (3), CAESAR assigns diverse frequencies to different sub-array antennas, as illustrated in Fig. 1.

The transmitted signal (14) can also be expressed by grouping the array elements which use the same frequency $\Omega_{n,k}$. Let $\boldsymbol{x}_{{\rm C},k}(n,t) \in \mathbb{C}^L$ with zero padding represent the portion of $\boldsymbol{x}_{\rm C}(n,t)$ which utilizes $\Omega_{n,k}$, i.e.,

$$\boldsymbol{x}_{{\rm C},k}(n,t) = \boldsymbol{P}(n,k)\boldsymbol{w}\left(\theta, \Omega_{n,k}\right) \phi\left(\Omega_{n,k}, t - nT_r\right), \tag{15}$$

where $\boldsymbol{P}(n,k) \in \{0,1\}^{L\times L}$ is a diagonal selection matrix with diagonal $\boldsymbol{p}(n,k) \in \{0,1\}^L$, whose l-th entry is one if the l-th array element transmits at frequency $\Omega_{n,k}$ and zero otherwise, i.e., $[\boldsymbol{P}(n,k)]_{l,l} = [\boldsymbol{p}(n,k)]_l = 1$ and $[\boldsymbol{x}_{{\rm C},k}(n,t)]_l = [\boldsymbol{x}_{\rm C}(n,t)]_l$ when $f_{n,l} = \Omega_{n,k}$. The transmitted signal is thus $\boldsymbol{x}_{\rm C}(n,t) := \sum_{k=0}^{K-1} \boldsymbol{x}_{{\rm C},k}(n,t)$, namely

$$\boldsymbol{x}_{\rm C}(n,t) = \sum_{k=0}^{K-1} \boldsymbol{P}(n,k)\boldsymbol{w}\left(\theta, \Omega_{n,k}\right) \phi\left(\Omega_{n,k}, t - nT_r\right). \tag{16}$$

Comparing (16) with (4), we find that each array element of CAESAR transmits a single frequency with unit amplitude while in WMAR all K frequencies with amplitudes scaled by a factor $1/\sqrt{K}$ are sent by each element.

Since all the antenna elements are utilized for the transmission, we have $\sum_{k=0}^{K-1} \boldsymbol{P}(n,k) = \boldsymbol{I}_L$. Without loss of generality, we assume that L/K is an integer and $\mathrm{tr}(\boldsymbol{P}(n,k)) = L/K$, where the trace of $\boldsymbol{P}(n,k)$ represents the number of antennas using the k-th frequency in the n-th pulse.

B. CAESAR Received Signal Model

We next model the received signal processed by CAESAR. Unlike WMAR, in which each antenna receives and separates different frequency components, in CAESAR, the l-th antenna element only receives radar returns at frequency $f_{n,l}$, and abandons other frequencies. This enables the use of narrowband receivers, simplifying the hardware requirements.

Note that the derivation of the signal component received at the k-th frequency in (6), $\tilde{x}_k(n,t)$, does not depend on the specific radar scheme. Here, substituting (15) into (6) yields

$$\tilde{x}_k(n,t) = \rho_{\mathrm{C}}(n,k,\delta_\vartheta)\phi\left(\Omega_{n,k}, t - nT_r - \frac{r(0)+nvT_r}{c}\right), \tag{17}$$

where $\rho_{\mathrm{C}}(n,k,\delta_\vartheta) := \boldsymbol{w}^H(\vartheta,\Omega_{n,k})\boldsymbol{P}(n,k)\boldsymbol{w}(\theta,\Omega_{n,k})$ is the transmit gain of the selected sub-array antenna, expressed as

$$\rho_{\mathrm{C}}(n,k,\delta_\vartheta) = \sum_{l=0}^{L-1} [\boldsymbol{p}(n,k)]_l \, e^{-j2\pi\Omega_{n,k} l d \delta_\vartheta / c}. \tag{18}$$

Note that, in contrast to the transmit gain of WMAR in (8) which tends to L, $\rho_{\mathrm{C}}(n,k,\delta_\vartheta)$ approaches L/K when $\delta_\vartheta \approx 0$. By repeating the arguments in the derivation of (10), the echo vector $\widetilde{\boldsymbol{y}}_{\mathrm{C},k}(n,t) \in \mathbb{C}^L$ can be written as

$$\begin{aligned}\widetilde{\boldsymbol{y}}_{\mathrm{C},k}(n,t) &= \beta \boldsymbol{w}^*\left(\vartheta,\Omega_{n,k}\right)\rho_{\mathrm{C}}(n,k,\delta_\vartheta)\\ &\quad \times \phi\left(\Omega_{n,k}, t - nT_r - (2r(0)+2nvT_r)/c\right).\end{aligned} \tag{19}$$

CAESAR receives and processes impinging signals by the corresponding elements of the antenna array. In particular, only a sub-array, whose elements are indicated by $\boldsymbol{P}(n,k)$, receives the impinging signal $\widetilde{\boldsymbol{y}}_{\mathrm{C},k}(n,t)$; the other array elements are tuned to other frequencies. The zero-padded received signal at the k-th frequency, denoted by $\boldsymbol{y}_{\mathrm{C},k}(n,t) \in \mathbb{C}^L$, is thus $\boldsymbol{y}_{\mathrm{C},k}(n,t) := \boldsymbol{P}(n,k)\widetilde{\boldsymbol{y}}_{\mathrm{C},k}(n,t)$. The full array received signal is given by $\boldsymbol{y}_{\mathrm{C}}(n,t) := \sum_{k=0}^{K-1}\boldsymbol{y}_{\mathrm{C},k}(n,t)$.

The observed signal $\boldsymbol{y}_{\mathrm{C}}(n,t)$ is sampled in a similar manner as detailed in Subsection II-C. Since CAESAR processes a single frequency component per antenna element, the measurements from each CRC are collected together as a data matrix $\boldsymbol{Y}_{\mathrm{C}} \in \mathbb{C}^{L\times N}$, as opposed to a $L\times N\times K$ cube processed by WMAR. By repeating the arguments used for obtaining (12), it holds that

$$[\boldsymbol{Y}_{\mathrm{C}}]_{l,n} = \tilde{\beta} e^{j\tilde{r}c_{n,k}} e^{j\tilde{v}n\zeta_{n,k}} e^{-j2\pi\Omega_{n,k} l d \sin\vartheta/c} \rho_{\mathrm{C}}(n,k,\delta_\vartheta), \tag{20}$$

which can be extended to account for multiple targets and noisy measurements as in (13), i.e.,

$$\begin{aligned}[\boldsymbol{Y}_{\mathrm{C}}]_{l,n} =& \sum_{s=0}^{S-1} \tilde{\beta}_s e^{j\tilde{r}_s c_{n,k}} e^{j\tilde{v}_s n\zeta_{n,k}} e^{-j2\pi\Omega_{n,k}\frac{ld\sin\vartheta_s}{c}}\\ & \times \rho_{\mathrm{C}}(n,k,\delta_{\vartheta_s}) + [\boldsymbol{N}]_{l,n},\end{aligned} \tag{21}$$

where $\boldsymbol{N} \in \mathbb{C}^{L\times N}$ is the additive noise. In order to recover the unknown parameters from the acquired data matrix (21), in the following section we present a dedicated recovery scheme.

IV. TARGET RECOVERY METHOD

Here, we present an algorithm for reconstructing the unknown HRR range, velocity, angle, and scattering intensity parameters of the scattering points from the radar measurements of both WMAR and CAESAR. Detection is performed based on the estimated scattering intensities. The detected scattering points may belong to either target or clutter, and they are identified by their Doppler estimates. The motivation for this approach is that in many ground-based radar systems, fast moving targets are of interest, while static or slow moving scatterers with zero or nearly zero Doppler are regarded as clutter. We henceforth model the Doppler of both targets and clutter as unknown parameters, which are simultaneously estimated. In specific applications where the clutter Doppler is a-priori known, one can apply clutter mitigation [20] in advance to the target recovery method. A similar procedure is also applied in pulse Doppler radars [19, Ch. 5.5.1], where the moving target indication filtering for gross clutter removal is placed prior to the pulse Doppler filter bank.

In order to maintain feasible computational complexity, we do not estimate all the parameters simultaneously: our proposed algorithm first jointly recovers the range-Doppler parameters followed by estimation of the unknown angles. When performing joint range-Doppler estimation, we assume that all the scattering points are located within the mainlobe of the transmit beam, and that the difference of the angle sine is negligible, i.e., $\delta_\vartheta \approx 0$. We then estimate the direction angles of scattering points based on their range-Doppler estimates.

We divide the target recovery method into three stages: 1) apply receive beamforming such that the magnitude of the received signal is enhanced, facilitating range-Doppler recovery; 2) apply CS methods for joint reconstruction of range and Doppler, followed by a target detection procedure; and 3) angle and scattering intensity estimation. These steps are discussed in Subsection IV-A-IV-C, respectively. A theoretical analysis of the range-Doppler estimation performance of our algorithm is provided in Section VI, where we quantify how using multiple carriers improves the range-Doppler reconstruction performance.

A. Receive Beamforming

The first step in processing the radar measurements is to beamform the received signal in order to facilitate recovery of the range-Doppler parameters. This receive beamforming is applied to radar returns at different frequencies separately. To formulate the beamforming technique, we henceforth focus on the k-th frequency of the n-th pulse, $\Omega_{n,k}$. For both CAESAR and WMAR, a total of L measurements correspond to $\Omega_{n,k}$, and are denoted by $\tilde{\boldsymbol{z}}_{n,k} \in \mathbb{C}^L$. For CAESAR, $\tilde{\boldsymbol{z}}_{n,k}$ is given by $\tilde{\boldsymbol{z}}_{n,k} = \boldsymbol{P}(n,k)[\boldsymbol{Y}_{\mathrm{C}}]_n$, of which only elements corresponding to the selected sub-array are nonzero. For WMAR, $\tilde{\boldsymbol{z}}_{n,k}$ consists of the entries $[\boldsymbol{Y}_{\mathrm{W}}]_{l,n,k}$ for each $l \in \mathcal{L}$. These measurements are integrated with the weights $\boldsymbol{w}(\theta,\Omega_{n,k})$ such that the receive beam is pointed towards θ, resulting in

$$Z_{k,n} := \boldsymbol{w}^T\tilde{\boldsymbol{z}}_{n,k} \in \mathbb{C}. \tag{22}$$

Define $\alpha_K := L^2/K^2$ for CAESAR, and $\alpha_K := L^2/\sqrt{K}$ for WMAR. When $\delta_{\vartheta_s} \approx 0$, i.e., the beam direction θ is close to the true angle of the target, the resulting beam pattern is simplified as in the following lemma, proved in Appendix A:

Lemma 1: If the difference of the angle sine satisfies $\delta_{\vartheta_s} \approx 0$, then $Z_{k,n}$ in (22) can be approximated as

$$Z_{k,n} \approx \alpha_K \sum_{s=0}^{S-1} \tilde{\beta}_s e^{j\tilde{r}_s c_{n,k}} e^{j\tilde{v}_s n \zeta_{n,k}}. \tag{23}$$

The receive beamforming produces the matrix $\boldsymbol{Z} \in \mathbb{C}^{K\times N}$ whose entries are $[\boldsymbol{Z}]_{k,n} := Z_{k,n}$, for each $k \in \mathcal{K}$, $n \in \mathcal{N}$. Under the approximation (23), the obtained $\boldsymbol{Z}$ is used for range-Doppler reconstruction, as discussed in the next subsection.

B. Range-Doppler Reconstruction Method

To reconstruct the range-Doppler parameters and detect targets in the presence of noise and/or clutter, we first recast the beamformed signal of Lemma 1 in matrix form, and apply CS methods to recover the unknown parameters, exploiting the underlying sparsity of the resulting model. The targets of interest are then identified based on the estimated parameters.

To obtain a sparse recovery problem, we start by discretizing the range and Doppler domains. Recall that $\tilde{r}_s$ and $\tilde{v}_s$ denote the normalized range and Doppler parameters, with resolutions $\frac{2\pi}{M}$ and $\frac{2\pi}{N}$, corresponding to the numbers of available frequencies and pulses, respectively. Both parameters belong to continuous domains in the unambiguous region $(\tilde{r}_s, \tilde{v}_s) \in [0, 2\pi)^2$. We discretize $\tilde{r}_s$ and $\tilde{v}_s$ into HRR and Doppler grids, denoted by grid sets $\mathcal{R} := \{\frac{2\pi m}{M} | m \in \mathcal{M}\}$ and $\mathcal{V} := \{\frac{2\pi n}{N} | n \in \mathcal{N}\}$, with grid intervals $\Delta_{\tilde{r}} = \frac{2\pi}{M}$ and $\Delta_{\tilde{v}} = \frac{2\pi}{N}$, respectively, and assume that the targets are located precisely on the grids. The target scene can now be represented by the matrix $\boldsymbol{B} \in \mathbb{C}^{M\times N}$ with entries

$$[\boldsymbol{B}]_{m,n} := \begin{cases} \tilde{\beta}_s \alpha_K, & \text{if } (\tilde{r}_s, \tilde{v}_s) = \left(\frac{2\pi m}{M}, \frac{2\pi n}{N}\right), \\ 0, & \text{otherwise.} \end{cases} \tag{24}$$

We can now use the sparse structure of (24) to formulate the range-Doppler reconstruction as a sparse recovery problem. To that aim, let $\boldsymbol{z} \in \mathbb{C}^{KN}$ and $\boldsymbol{\beta} \in \mathbb{C}^{MN}$ be the vectorized representations of $\boldsymbol{Z}$ and $\boldsymbol{B}$, respectively, i.e., $[\boldsymbol{z}]_{k+nK} = Z_{k,n}$ and $[\boldsymbol{\beta}]_{n+mN} := [\boldsymbol{B}]_{m,n}$. From (23), it holds that

$$\boldsymbol{z} = \boldsymbol{\Phi}\boldsymbol{\beta}, \tag{25}$$

where the entries of $\boldsymbol{\Phi} \in \mathbb{C}^{KN\times MN}$ are given by

$$[\boldsymbol{\Phi}]_{k+nK, l+mN} := e^{j\frac{2\pi m}{M}c_{n,k} + j\frac{2\pi l}{N} n\zeta_{n,k}}, \tag{26}$$

$m \in \mathcal{M}$, $l, n \in \mathcal{N}$, and $k \in \mathcal{K}$. The matrix $\boldsymbol{\Phi}$ is determined by the frequencies utilized in each pulse. Consequently, $\boldsymbol{\Phi}$ is a random matrix, as these parameters are randomized by the radar transmitters, whose realization is known to the receiver.

In the presence of noisy radar returns, (25) becomes

$$\boldsymbol{z} = \boldsymbol{\Phi}\boldsymbol{\beta} + \boldsymbol{n}, \tag{27}$$

where the entries of the noise vector $\boldsymbol{n} \in \mathbb{C}^{KN}$ are the beamformed noise, e.g., for CAESAR these are given by $[\boldsymbol{n}]_{k+nK} = \boldsymbol{w}^T(\theta, \Omega_{n,k})\boldsymbol{P}(n,k)[\boldsymbol{N}]_n$.

Since in each pulse only a subset of the available frequencies are transmitted, i.e., $K \leq M$, the sensing matrix $\boldsymbol{\Phi}$ in (27) has more columns than rows, $MN \geq KN$, indicating that solving (27) is naturally an under-determined problem. When $\boldsymbol{\beta}$ is S-sparse, which means that there are at most S non-zeroes in $\boldsymbol{\beta}$ and $S \ll MN$, CS algorithms can be used to solve (27), yielding the estimate $\hat{\boldsymbol{\beta}}$.

Particularly, CS methods aim to solve under-determined problems such as (25) by seeking the sparsest solution, i.e.,

$$\hat{\boldsymbol{\beta}} = \arg\min_{\boldsymbol{\beta}} \|\boldsymbol{\beta}\|_0, \text{ s.t. } \boldsymbol{z} = \boldsymbol{\Phi}\boldsymbol{\beta}. \tag{28}$$

The ℓ_0 optimization in (28) is generally NP-hard. To reduce computational complexity, many alternatives including ℓ_1 optimization and greedy approaches have been suggested to approximate (28), see [21].

We take ℓ_1 optimization as an example, under which we provide a theoretical analysis and numerically evaluate the performance in Sections VI and VII, respectively. In particular, in the absence of noise, we use the basis pursuit algorithm, which solves

$$\hat{\boldsymbol{\beta}} = \arg\min_{\boldsymbol{\beta}} \|\boldsymbol{\beta}\|_1, \text{ s.t. } \boldsymbol{z} = \boldsymbol{\Phi}\boldsymbol{\beta}, \tag{29}$$

instead of (28). In noisy cases, recovering $\boldsymbol{\beta}$ can be formulated as minimizing the ℓ_1 norm under a ℓ_2 constraint on the fidelity:

$$\hat{\boldsymbol{\beta}} = \arg\min_{\boldsymbol{\beta}} \|\boldsymbol{\beta}\|_1, \text{ s.t. } \|\boldsymbol{z} - \boldsymbol{\Phi}\boldsymbol{\beta}\|_2 \leq \eta. \tag{30}$$

Problem (30) can be solved using the Lasso method [21], which applies the ℓ_1 regularized least squares as

$$\hat{\boldsymbol{\beta}} = \arg\min_{\boldsymbol{\beta}} \lambda \|\boldsymbol{\beta}\|_1 + \frac{1}{2}\|\boldsymbol{z} - \boldsymbol{\Phi}\boldsymbol{\beta}\|_2^2, \tag{31}$$

where η and λ are predefined parameters.

Having obtained the estimate $\hat{\boldsymbol{\beta}}$ using CS methods, we can use it to identify which of these estimated parameters correspond to a true target of interest. Elements with significant amplitudes in $\hat{\boldsymbol{\beta}}$ are detected as dominant scattering points. Denote by $\widehat{\mathcal{S}}$ the support set indexing these dominant scattering points, whose range-Doppler parameters are recovered from the corresponding indices in $\widehat{\mathcal{S}}$. For example, we may use some threshold T_h to determine whether the amplitude is significant[19, Ch. 6]. In this case, the support set is given by $\widehat{\mathcal{S}} = \{s | |[\boldsymbol{\beta}]_s| > T_h\}$. According to their Doppler estimates, these dominant scattering points are categorized into target of interests or clutter individually.

With the recovered range-Doppler values, one can estimate the angle and refine the scattering intensity, as detailed in the following subsection.

C. Angle and Scattering Intensity Estimation

In this part, we refine the angle estimation of the scattering points, which are coarsely assumed within the transmit beam in the receive beamforming step, i.e., $\delta_\vartheta \approx 0$. While the following formulation focuses on CAESAR, the resulting algorithm is also applicable for WMAR as well as FAR.

We estimate the directions of the scatterers individually, as different points may have different direction angles. Since after receive beamforming some directional information is lost in $\boldsymbol{Z}$, we recover the angles from the original data matrix $\boldsymbol{Y}_{\mathrm{C}}$ (21). Using the obtained range and Doppler estimates, we first isolate echoes for each scattering point with an orthogonal projection, and apply a matched filter to estimate the direction angle of each scattering point. Finally, we use least squares to infer the scattering intensities.

1) Echo Isolation Using Orthogonal Projection: In order to accurately estimate the angle of each scattering point, it is necessary to mitigate the interference between scattering points.

To that aim, we use an orthogonal projection to isolate echoes from each scatterer.

Let $\widehat{\mathcal{S}}$ be the support set of $\hat{\boldsymbol{\beta}}$, and infer the normalized range and Doppler parameters $\{\tilde{r}_s, \tilde{v}_s\}$ from $\widehat{\mathcal{S}}$. According to (21), given these parameters, the original data vector from the l-th array element can be written as $[\boldsymbol{Y}_{\rm C}^T]_l = [\boldsymbol{\Psi}_l]_{\widehat{\mathcal{S}}}[\boldsymbol{\gamma}_l]_{\widehat{\mathcal{S}}} + [\boldsymbol{N}^T]_l$, where $\boldsymbol{\Psi}_l \in \mathbb{C}^{N\times MN}$ has entries $[\boldsymbol{\Psi}_l]_{n,s} := e^{j\tilde{r}_s c_{n,k}} e^{j\tilde{v}_s n\zeta_{n,k}}$, and $\boldsymbol{\gamma}_l \in \mathbb{C}^{MN}$ denotes the effective scattering intensities corresponding to all discrete range-Doppler grids, with s-th entry $[\boldsymbol{\gamma}_l]_s := \tilde{\beta}_s \rho(n,k,\delta_{\vartheta_s}) e^{-j2\pi\Omega_{n,k} l d \sin\vartheta_s / c}$. The intensities, containing unknown phase shifts and antenna gains due to angles ϑ_s, are estimated as $[\hat{\boldsymbol{\gamma}}_l]_{\widehat{\mathcal{S}}} = \arg\min_{[\boldsymbol{\gamma}_l]_{\widehat{\mathcal{S}}}} \left\| [\boldsymbol{Y}_{\rm C}^T]_l - [\boldsymbol{\Psi}]_{\widehat{\mathcal{S}}} [\boldsymbol{\gamma}_l]_{\widehat{\mathcal{S}}} \right\|_2^2 = [\boldsymbol{\Psi}]_{\widehat{\mathcal{S}}}^{\dagger} [\boldsymbol{Y}_{\rm C}^T]_l$, where $\boldsymbol{A}^{\dagger} = (\boldsymbol{A}^H\boldsymbol{A})^{-1}\boldsymbol{A}^H$ and we assume that $|\widehat{\mathcal{S}}| < N$ and $\boldsymbol{A}^H\boldsymbol{A}$ is invertible. The received radar echo from the s-th scattering point, $\widehat{\boldsymbol{Y}}_s \in \mathbb{C}^{L\times N}$, $s \in \widehat{\mathcal{S}}$, is then reconstructed by setting the l-th row as

$$\left[\widehat{\boldsymbol{Y}}_s^T\right]_l = [\boldsymbol{\Psi}]_s \, [\hat{\boldsymbol{\gamma}}_l]_s . \tag{32}$$

2) Angle Estimation Using Matched Filter: With the isolated echoes $\widehat{\boldsymbol{Y}}_s$ of the s-th scattering point, we use a matched filter to refine the unknown angle ϑ_s, which is coarsely assumed within the beam in the previous receive beamforming procedure, i.e., $\vartheta_s \in \vartheta := \theta + [-\frac{\pi}{2L}, \frac{\pi}{2L}]$. Using (21), we write the isolated echo as $\widehat{\boldsymbol{Y}}_s = \tilde{\beta}_s \boldsymbol{Y}_s(\vartheta_s) + \boldsymbol{N}_s$, where $\boldsymbol{N}_s$ denotes the noise matrix corresponding to the s-th scattering point. The entries of the steering matrix $\boldsymbol{Y}_s(\vartheta_s) \in \mathbb{C}^{L\times N}$ are

$$[\boldsymbol{Y}_s(\vartheta_s)]_{l,n} := \rho_{\rm C}(n,k,\delta_{\vartheta_s}) e^{j\tilde{r}_s c_{n,k}} e^{j\tilde{v}_s n\zeta_{n,k}} e^{-j2\pi\Omega_{n,k} l d \sin\vartheta_s / c},$$

which can be computed using (18) with given ϑ_s and the estimates of the range-Doppler parameters. Note that $\tilde{\beta}_s$, ϑ_s and $\boldsymbol{N}_s$ are unknown, and ϑ_s is of interest. The value of the intensity $\tilde{\beta}_s$ recovered next is refined in the sequel to improve accuracy. Here, we apply least squares estimation, i.e.,

$$\hat{\vartheta}_s, \hat{\tilde{\beta}}_s = \mathop{\arg\min}_{\vartheta_s, \tilde{\beta}_s} \left\| \mathrm{vec}\left(\widehat{\boldsymbol{Y}}_s\right) - \tilde{\beta}_s \mathrm{vec}\left(\boldsymbol{Y}_s(\vartheta_s)\right) \right\|_2^2. \tag{33}$$

Substituting $\hat{\tilde{\beta}}_s = (\mathrm{vec}(\boldsymbol{Y}_s(\vartheta_s)))^{\dagger} \mathrm{vec}(\widehat{\boldsymbol{Y}}_s) = \frac{\mathrm{tr}(\boldsymbol{Y}_s^H(\vartheta_s)\widehat{\boldsymbol{Y}}_s)}{\|\boldsymbol{Y}_s(\vartheta_s)\|_F^2}$ into (33) yields a matched filter

$$\hat{\vartheta}_s = \mathop{\arg\max}_{\vartheta_s \in \vartheta} \left| \mathrm{tr}\left(\boldsymbol{Y}_s^H(\vartheta_s)\widehat{\boldsymbol{Y}}_s\right) \right|^2 / \|\boldsymbol{Y}_s(\vartheta_s)\|_F^2. \tag{34}$$

The angle $\hat{\vartheta}_s$ is estimated for each $s \in \widehat{\mathcal{S}}$ via (34) separately.

3) Scattering Intensity Estimation Using Least Squares: When $\delta_{\vartheta_s} \neq 0$, there exist approximation errors in (23) and the resultant intensity estimate $\hat{\boldsymbol{\beta}}$. We thus propose to refine the estimation of $\boldsymbol{\beta}$ from the original data matrix $\boldsymbol{Y}_{\rm C}$ once the range-Doppler and angle parameters are acquired. Given estimated angles $\hat{\vartheta}_s$, we concatenate the steering vectors into $\boldsymbol{C} := [\mathrm{vec}(\boldsymbol{Y}_{s_0}(\hat{\vartheta}_{s_0})), \mathrm{vec}(\boldsymbol{Y}_{s_1}(\hat{\vartheta}_{s_1})), \ldots]$, $s_0, s_1, \cdots \in \widehat{\mathcal{S}}$. The model (21) is rewritten as $\mathrm{vec}(\boldsymbol{Y}_{\rm C}) = \boldsymbol{C}[\boldsymbol{\beta}]_{\widehat{\mathcal{S}}} + \boldsymbol{N}$, and $\boldsymbol{\beta}$ can be re-estimated via least squares as

$$\left[\hat{\boldsymbol{\beta}}\right]_{\widehat{\mathcal{S}}} = \mathop{\arg\min}_{[\boldsymbol{\beta}]_{\widehat{\mathcal{S}}}} \left\| \mathrm{vec}\left(\boldsymbol{Y}_{\rm C}\right) - \boldsymbol{C}\left[\boldsymbol{\beta}\right]_{\widehat{\mathcal{S}}} \right\|_2^2 = \boldsymbol{C}^{\dagger} \mathrm{vec}\left(\boldsymbol{Y}_{\rm C}\right). \tag{35}$$

The parameter estimation method is summarized as Algorithm 1.

Algorithm 1: CAESAR Target Recovery.

```
Input: Data matrix $\boldsymbol{Y}_{\rm C}$.
Beamform $\boldsymbol{Y}_{\rm C}$ into $\boldsymbol{Z}$ via (22).
Use CS methods to recover the indices of the dominant elements of $\boldsymbol{\beta}$, representing the parameters of the targets of interest, denoted by $\widehat{\mathcal{S}}$, from $\boldsymbol{Z}$ based on the sensing matrix $\boldsymbol{\Phi}$ (26).
Reconstruct the normalized range-Doppler parameters $\{\tilde{r}_s, \tilde{v}_s\}$ from $\widehat{\mathcal{S}}$ based on (24).
Isolate $\boldsymbol{Y}_{\rm C}$ into multiple echoes $\{\widehat{\boldsymbol{Y}}_s\}$ via (32).
Recover the angles $\{\vartheta_s\}$ from $\{\widehat{\boldsymbol{Y}}_s\}$ via (34).
Refine the scattering intensities $\{\beta_s\}$ using (35).
Output: parameters $\{\tilde{r}_s, \tilde{v}_s, \vartheta_s, \tilde{\beta}_s\}$.
```

V. COMPARISON TO RELATED RADAR SCHEMES

We next compare our proposed WMAR and CAESAR schemes, and discuss their relationship with relevant previously proposed radar methods.

A. Comparison of WMAR, CAESAR, and FAR

We compare our proposed techniques to each other, as well as to FAR, which is a special case of both WMAR and CAESAR obtained by setting $K = 1$. We focus on the following aspects: 1) instantaneous bandwidth; 2) the number of measurements in a CPI; and 3) signal-to-noise ratio (SNR). A numerical comparison of the target recovery performance of the considered radar schemes is provided in Section VII.

In terms of instantaneous bandwidth, recall that CAESAR and FAR use narrowband transceivers, and a monotone signal is transmitted or received by each element. In WMAR, K multitone signals are sent and received simultaneously in each pulse, thus it requires instantaneous wideband components.

To compare the number of obtained measurements, we note that for each CRC, WMAR acquires a data cube with NLK samples, while FAR and CAESAR collect NL samples in the data matrix. After receive beamforming, the number of observations become N, NK and NK, for FAR, CAESAR, and WMAR, respectively, via (22). This indicates that the multicarrier waveforms of CAESAR and WMAR increase the number of measurements after receive beamforming.

The aforementioned radar schemes also differ in their SNR, as the transmitted power and antenna gains differ. Here, as in [19, Page 304, Ch. 6], SNR refers to the ratio of the power of the signal component to the power of the noise component after coherently accumulating the radar returns. To see this difference, we consider the case when there exists a target with range-Doppler-angle $(0, 0, 0)$, scattering coefficient β and the noise elements in $\boldsymbol{N}$ are i.i.d. zero-mean proper-complex Gaussian with variance σ^2. In this case, coherent accumulation of radar returns reduces to $\sum_{l,n,k} [\boldsymbol{Y}_{\rm W}]_{l,n,k}$ in WMAR and $\sum_{l,n} [\boldsymbol{Y}_{\rm C}]_{l,n}$ in CAESAR (FAR can be regarded as a special case of WMAR/CAESAR with $K = 1$), and the antenna gains are $\rho_{\rm W} = L$ and $\rho_{\rm C} = L/K$, respectively. It follows from (13) that the signal amplitude in radar returns of WMAR is $L|\beta|/\sqrt{K}$. After coherent accumulation, the amplitude becomes

$NLK \cdot L|\beta|/\sqrt{K}$, leading to a signal power of $N^2L^4K|\beta|^2$, while the power of the noise component becomes $NLK \cdot \sigma^2$. Hence, the SNR of WMAR is $NL^3|\beta|^2/\sigma^2$. In CAESAR, the amplitude of the signal component in $\boldsymbol{Y}_{\mathrm{C}}$ is $L/K|\beta|$, which becomes $NL \cdot L/K|\beta|$ after accumulation. Since there are only NL noise elements in CAESAR, the noise power after accumulation is $NL \cdot \sigma^2$ and the resultant SNR is $NL^3|\beta|^2/(K^2\sigma^2)$. Letting $K = 1$ implies that the SNR of FAR is also $NL^3|\beta|^2/\sigma^2$. The SNR calculation indicates that CAESAR has an SNR loss by a factor of K^2 compared to WMAR and FAR. This loss stems from the fact that CAESAR uses a subset of the antenna array for each carrier, and thus has lower antenna gain than FAR and WMAR. This SNR reduction can affect the performance of CAESAR in the presence of noise, as numerically demonstrated in Section VII.

The above comparison reveals the tradeoff between instantaneous bandwidth requirement, number of observations, and post-accumulation SNR. Among these three factors, the number of observations is crucial to the target recovery performance especially in complex electromagnetic environments, where some observations may be discarded due to strong interference [8]. The proposed multi-carrier schemes, WMAR and CAESAR, are numerically shown to outperform FAR in Section VII, despite the gain loss of CAESAR. CAESAR also achieves performance within a relatively small gap compared to WMAR, while avoiding the usage of instantaneous wideband components. The resulting tradeoff between number of beamformed observations and SNR, induced by the selection of K, is not the only aspect which must be accounted for when setting the value of K, as it also affects the frequency agility profile. In particular, smaller K values result in increased spectral flexibility, as different pulses are more likely to use non-overlapping frequency sets. Consequently, in our numerical analysis in Section VII we use small values of K, for which the gain loss between CAESAR and WMAR is less significant, and increased frequency agility is maintained. In addition, CAESAR can also exploit its spatial agility character, which is not present in FAR or WMAR, to realize a DFRC system, as discussed in our companion paper [17].

B. Comparison to Previously Proposed Schemes

Similarly to CAESAR, previously proposed FDMA-MIMO radar [9], SUMMeR [11], and FDA radar [12], [13] schemes also transmit a monotone waveform from each antenna element while different elements simultaneously transmit multiple carrier frequencies. The main differences between our approaches and these previous methods are beam pattern and frequency agility. Due to the transmission of diverse carrier frequencies from different array elements of FDMA-MIMO/SUMMeR/FDA, the array antenna does not form a focused transmit beam and usually illuminates a large field-of-view [14]. This results in a transmit gain loss which degrades the performance, especially for track mode, where a high-gain directional beam is preferred [14]. By transmitting each selected frequency with an antenna array (the full array in WMAR and a sub-array in CAESAR), our methods achieve a focused beam pattern that facilitates accurate target recovery.

Furthermore, FDMA-MIMO and FDA transmit all available frequencies simultaneously, and thus do not share the advantages of frequency agility, e.g., improved ECCM and EMC performance, as the multi-carrier version of SUMMeR and the proposed WMAR/CAESAR. In addition, FDMA-MIMO, SUMMeR and WMAR receive instantaneous wideband signals with every single antenna, as opposed to FDA [13] and CAESAR, which use narrowband receivers.

To summarize, we compare in Table I the main characteristics of these radar schemes. Unlike previously proposed radar methods, our proposed techniques are based on phased array antenna and frequency agile waveforms to achieve directional transmit beam and high resistance against interference. In terms of instantaneous bandwidth, CAESAR is preferred for its usage of monotone waveforms and simple instantaneous narrowband receiver.

VI. PERFORMANCE ANALYSIS OF RANGE-DOPPLER RECONSTRUCTION

Range-Doppler reconstruction plays a crucial role in target recovery. This section presents a theoretical analysis of range-Doppler recovery using CS. Since both WMAR and CAESAR are generalizations of FAR, the following analysis is inspired by the study of CS-based FAR recovery in [7]. In particular, we extend the results of [7] to multi-carrier waveforms, as well as to extremely complex electromagnetic environments, where some transmitted pulses are interfered by intentional or unintentional interference. In the presence of such interference, only partial observations in the beamformed matrix $\boldsymbol{Z}$ remain effective for range-Doppler reconstruction. To present the analysis, we first briefly review some basic analysis techniques of CS in Subsection VI-A, followed by the range-Doppler recovery performance analysis in Subsection VI-B.

A. Preliminaries

There have been extensive studies on theoretical conditions that guarantee unique recovery for noiseless models or robust recovery for noisy models [21]. The majority of these studies characterize conditions and properties of the measurement matrix $\boldsymbol{\Phi}$, including spark, mutual incoherence property (MIP) and restricted isometry property (RIP).

Following [7], we focus on the MIP. A sensing matrix $\boldsymbol{\Phi}$ is said to satisfy the MIP when its coherence, defined as

$$\mu(\boldsymbol{\Phi}) := \max_{i\neq j} \left|[\boldsymbol{\Phi}]_i^H\, [\boldsymbol{\Phi}]_j\right| / \left(\|\, [\boldsymbol{\Phi}]_i \,\|_2 \|\, [\boldsymbol{\Phi}]_j \,\|_2\right), \qquad (36)$$

is not larger than some predefined threshold. Bounded coherence ensures unique or robust recovery using a variety of computationally efficient CS methods. We take ℓ_1 optimization as an example to explain the bounds on matrix coherence. In the absence of noise, the uniqueness of the solution to (29) is guaranteed by the following theorem:

Theorem 2 ([22])*:* Suppose the sensing matrix $\boldsymbol{\Phi}$ has coherence $\mu(\boldsymbol{\Phi}) < \frac{1}{2S-1}$. If $\boldsymbol{\beta}$ solves (29) and has support size at most S, then $\boldsymbol{\beta}$ is the unique solution to (29).

In noisy cases, the following result shows that $\mu(\boldsymbol{\Phi}) < \frac{1}{2S-1}$ also guarantees stable recovery.

Theorem 3 ([23])*:* Consider the model (27) with $\|\boldsymbol{z}\|_2 \le \epsilon \le \eta$ and $\|\boldsymbol{\beta}\|_0 \le S$, and let sensing matrix $\boldsymbol{\Phi}$ have coherence $\mu(\boldsymbol{\Phi}) < \frac{1}{2S-1}$. If $\hat{\boldsymbol{\beta}}$ solves (30), then

$$\|\hat{\boldsymbol{\beta}} - \boldsymbol{\beta}\|_2 \le \sqrt{3(1+\mu)}(\eta+\epsilon)/\left(1-(2S-1)\mu\right). \qquad (37)$$

TABLE I
COMPARISON BETWEEN RADAR SCHEMES

Characters	Frequency agility	Beam pattern	# of observation	Transmit bandwidth	Receive bandwidth
WMAR	**Yes**	**Focused**	Moderate	Large	Large
CAESAR	**Yes**	Moderately focused	Moderate	**Small**	**Small**
FAR	**Yes**	**Focused**	Small	**Small**	**Small**
FDMA-MIMO	No	Omnidirectional	**Large**	**Small**	Large
SUMMeR	**Yes**	Omnidirectional	Moderate	**Small**	Large
FDA	No	Omnidirectional	**Large**	**Small**	**Small**

Based on Theorems 2 and 3, we next analyze the coherence measure of the sensing matrix $\boldsymbol{\Phi}$ in (26) for CAESAR and WMAR (whose sensing matrices are identical), and establish the corresponding performance guarantees.

B. Performance Analysis

Here, we analyze the range-Doppler reconstruction of WMAR and CAESAR. Since the sensing matrix $\boldsymbol{\Phi}$ is random, we start by analyzing its statistics, and then derive conditions that ensure unique recovery by invoking Theorem 2.

We assume that the frequency set $\mathcal{F}_n$ is uniformly i.i.d. over $\{\mathcal{X}|\mathcal{X}\subset\mathcal{F},|\mathcal{X}|=K\}$. For mathematical convenience, in our analysis we adopt the narrow relative bandwidth assumption from [7], i.e., $\zeta_{n,k}\approx 1$, such that (26) becomes

$$[\boldsymbol{\Phi}]_{k+nK,l+mN} = e^{j\frac{2\pi m}{M}c_{n,k}+j\frac{2\pi l}{N}n}. \tag{38}$$

Numerical results in [7] indicate that large relative bandwidth has negligible effect on the MIP of $\boldsymbol{\Phi}$. In addition, recall that all the targets precisely lie on the predefined grid points, as assumed in Subsection IV-B. Here, we adopt the on-the-grid assumption for mathematical convenience. Consequently, the accuracy and actual resolutions of range and Doppler reconstruction results are restricted by the grid intervals, i.e., $2\pi/M$ and $2\pi/N$, respectively. In practical scenarios, we may use denser grid points, as will be discussed by simulations in Subsection VII-B. Denser grid enhances the obtainable accuracy/resolution and alleviates the performance loss when the real parameters are off the grid points. However, the density of grid points cannot go to infinity, because denser grid affects the incoherence property of the observation matrix while increasing the memory requirements and the computational burden. An alternative approach to overcome the need to specify a range-Doppler grid is to utilize off-the-grid CS methods, see [24].

In complex electromagnetic environments, some of the radar echoes may be corrupted due to jamming or interference. Heavily corrupted echoes are unwanted and should be removed before processing in order to avoid their influence on the estimation of target parameters [8]. In this case, the corrupted radar returns are identified, as such echoes typically have distinct characters, e.g., extremely large amplitudes. These interfered observations are regarded as missing, where we consider two kinds of missing patterns: 1) pulse selective, i.e., all observations in certain pulses are missing, which happens when the interference in these pulses is intense over all sub-bands; 2) observation selective, namely, only parts of the observations are missed when the corresponding pulse is interfered. We consider the first case, assuming that the radar receiver knows which pulses are corrupted, and leave the analysis under the second case for future investigation. In particular, we adopt the missing-or-not approach [25], in which each pulse in $\boldsymbol{z}$ has a probability of $1-u$, $0<u<1$, to be corrupted, and the missing-or-not status of the pulses are statistically independent of each other.

After removing the corrupted returns, only part of the observations in the beamformed vector $\boldsymbol{z}$ (27) are used for range-Doppler recovery. Equivalently, corresponding rows in $\boldsymbol{\Phi}$ can be regarded as missing, affecting the coherence of the matrix and thus the reconstruction performance. Denote by $\Lambda\subset\mathcal{N}$ the random set of available pulse indexes and by $\Lambda_* := \{nK+k|n\in\Lambda,k\in\mathcal{K}\}$ the corresponding index set of available observations. The signal model (27) is now

$$\boldsymbol{z}_* = \boldsymbol{\Phi}_*\boldsymbol{\beta}+\boldsymbol{n}_*, \tag{39}$$

where $\boldsymbol{z}_* := [\boldsymbol{z}]_{\Lambda_*}$, $\boldsymbol{\Phi}_* := [\boldsymbol{\Phi}^T]_{\Lambda_*}^T$, and $\boldsymbol{n}_* := [\boldsymbol{n}]_{\Lambda_*}$.

Consider the inner product of two columns in $\boldsymbol{\Phi}_*$, denoted $[\boldsymbol{\Phi}_*]_{l_1}$ and $[\boldsymbol{\Phi}_*]_{l_2}$, corresponding to grid points $(\frac{2\pi m_1}{M},\frac{2\pi n_1}{N})$ and $(\frac{2\pi m_2}{M},\frac{2\pi n_2}{N})$, respectively, $l_1,l_2\in 0,1,\ldots,MN-1$, $m_1,m_2\in\mathcal{M}$, $n_1,n_2\in\mathcal{N}$. While there are M^2N^2 different pairs of (l_1,l_2), the magnitude of the inner product $\left|[\boldsymbol{\Phi}_*]_{l_1}^H[\boldsymbol{\Phi}_*]_{l_2}\right|$, which determines the coherence of $\boldsymbol{\Phi}_*$, takes at most $MN-1$ distinct random values. To see this, note that

$$\begin{aligned}[\boldsymbol{\Phi}_*]_{l_1}^H[\boldsymbol{\Phi}_*]_{l_2} &= \sum_{n\in\Lambda}\sum_{k=0}^{K-1} e^{-j\frac{2\pi m_1}{M}c_{n,k}-j\frac{2\pi n_1}{N}n}e^{j\frac{2\pi m_2}{M}c_{n,k}+j\frac{2\pi n_2}{N}n}\\ &= \sum_{n\in\Lambda}\sum_{k=0}^{K-1} e^{-j2\pi\frac{m_1-m_2}{M}c_{n,k}-j2\pi\frac{n_1-n_2}{N}n},\end{aligned} \tag{40}$$

indicating that the inner product depends only on the difference of the grid points, i.e., m_1-m_2 and n_1-n_2, and not on the individual values of the column indices l_1 and l_2. It follows from (40) that the MIP of $\boldsymbol{\Phi}_*$ can be written as

$$\mu(\boldsymbol{\Phi}_*) = \max_{\substack{(\Delta_m,\Delta_n)\\ \neq(0,0)}}\frac{1}{|\Lambda|K}\sum_{n\in\Lambda}\sum_{k=0}^{K-1}e^{-j\Delta_m c_{n,k}}e^{-j\Delta_n n}. \tag{41}$$

where $\Delta_m := 2\pi\frac{m_1-m_2}{M}$, $\Delta_n := 2\pi\frac{n_1-n_2}{N}$ take values in the sets $\Delta_m\in\{\pm\frac{2\pi m}{M}\}_{m\in\mathcal{M}}$ and $\Delta_n\in\{\pm\frac{2\pi n}{N}\}_{n\in\mathcal{N}}$, respectively.

Next, we define

$$\chi_n(\Delta_m,\Delta_n) := I_\Lambda(n)\frac{1}{K}\sum_{k=0}^{K-1}e^{-j\Delta_m c_{n,k}-j\Delta_n n}, \tag{42}$$

where the random variable $I_\Lambda(n)$ satisfies $I_\Lambda(n)=1$ when $n\in\Lambda$ and 0 otherwise. In addition, let $\chi(\Delta_m,\Delta_n) := \sum_{n=0}^{N-1}\chi_n(\Delta_m,\Delta_n)$. Some of the magnitudes $|\chi(\Delta_m,\Delta_n)|$ are duplicated since $\chi(\Delta_m,\Delta_n)=\chi(\Delta_m\pm 2\pi,\Delta_n\pm 2\pi)$ and $\chi(\Delta_m,\Delta_n)=\chi^*(-\Delta_m,-\Delta_n)$. To eliminate the duplication and remove the trivial nonrandom value $\chi(0,0)$, we restrict the values of Δ_m and Δ_n to $\Delta_m\in\{\frac{2\pi m}{M}\}_{m\in\mathcal{M}}$ and $\Delta_n\in\{\frac{2\pi n}{N}\}_{n\in\mathcal{N}}$, respectively, and define the set $\Xi := \{(\Delta_m,\Delta_n)|(m,n)\in\mathcal{M}\times\mathcal{N}\backslash(0,0)\}$, with cardinality $|\Xi| = MN-1$, such that each value of $\left|[\boldsymbol{\Phi}_*]_{l_1}^H[\boldsymbol{\Phi}_*]_{l_2}\right|$ (except the trivial case $l_1 = l_2$) corresponds to a single element of the set Ξ. We can now write (41) as

$$\mu(\mathbf{\Phi}_*) = \max_{(\Delta_m,\Delta_n)\in\Xi} \left|\chi\left(\Delta_m,\Delta_n\right)\right| / |\Lambda|. \tag{43}$$

The coherence in (43) is a function of the dependent random variables χ and $|\Lambda|$. To bound μ, we derive bounds on χ and $|\Lambda|$, respectively. To this aim, we first characterize the statistical moments of $\chi_n(\Delta_m,\Delta_n)$ for some fixed $(\Delta_m,\Delta_n)\in\Xi$, which we denote henceforth as χ_n, in the following lemma:

Lemma 4: The sequence of random variables $\{\chi_n\}$ satisfies

$$\mathrm{E}\left[\chi_n\right] = \begin{cases} ue^{j\Delta_n n}, & \text{if } \Delta_m = 0, \\ 0, & \text{otherwise,} \end{cases} \tag{44}$$

$$\sum_{n=0}^{N-1} \mathrm{D}\left[\chi_n\right] = \begin{cases} u(1-u)N, & \text{if } \Delta_m = 0, \\ \frac{M-K}{(M-1)K}uN, & \text{otherwise.} \end{cases} \tag{45}$$

Furthermore, for each $n\in\mathcal{N}$,

$$|\chi_n - \mathrm{E}[\chi_n]| \le 1, \quad \text{w.p. } 1. \tag{46}$$

Proof: See Appendix B. ■

Using Lemma 4, the probability that the magnitude $|\chi|$ is bounded can be derived as in the following Corollary:

Corollary 5: Let $V := \max\{u(1-u)N, \frac{M-K}{(M-1)K}uN\}$. For any $(\Delta_m,\Delta_n)\in\Xi$ and $\epsilon \le V$ it holds that $\mathbb{P}(|\chi| \ge \sqrt{V}+\epsilon) \le e^{-\frac{\epsilon^2}{4V}}$.

Proof: Based on the definition (42) and the independence assumption on the frequency selection and missing-or-not status of each pulse, it holds that $\{\chi_n - \mathrm{E}[\chi_n]\}_{n\in\mathcal{N}}$ are independent zero-mean complex-valued random variables. Now, since $\sum_{n=0}^{N-1}\mathrm{E}[\chi_n] = u\sum_{n=0}^{N-1}e^{j\Delta_n n}$ when $\Delta_m = 0$ and 0 otherwise according to (44), and $\sum_{n=0}^{N-1}e^{j\Delta_n n} = \frac{1-e^{j\Delta_n N}}{1-e^{j\Delta_n}}$ equals 0 for $\Delta_n \in \{\frac{2\pi n}{N}\}_{n\in\mathcal{N}\backslash\{0\}}$, recalling that $(\Delta_m,\Delta_n)\neq(0,0)$, we have $\sum_{n=0}^{N-1}\mathrm{E}[\chi_n] = 0$. Then, it holds that $\sum_{n=0}^{N-1}(\chi_n - \mathrm{E}[\chi_n]) = \sum_{n=0}^{N-1}\chi_n = \chi$. Combining Bernstein's inequality [26, Thm. 12] with the fact that by (46), $|\chi_n - \mathrm{E}[\chi_n]| \le 1$, results in this corollary.

We next derive a bound on the number of effective pulses $|\Lambda|$ in the following lemma:

Lemma 6: For any $t > 0$, $\mathbb{P}(|\Lambda| \le uN - t) < e^{-\frac{2t^2}{N}}$.

Proof: Since, by its definition, $|\Lambda|$ obeys a binomial distribution, this lemma is a direct consequence of [27, Thm. 1]. ■

Based on the requirement $\mu(\mathbf{\Phi}_*) > \frac{1}{2K-1}$ in Theorem 2, we now use Corollary 5 and Lemma 6 to derive a sufficient condition on the radar parameters M, N, K, as well as the intensity of interference $1-u$, guaranteeing that the measurement matrix $\mathbf{\Phi}_*$ meets the requirement with high probability. This condition is stated in the following theorem:

Theorem 7: For any constant $\delta > 0$, the coherence of $\mathbf{\Phi}_*$ satisfies $\mathbb{P}(\mu(\mathbf{\Phi}_*) \le \frac{1}{2S-1}) \ge 1-\delta$ when

$$S \le \frac{uN/\sqrt{V}}{1+\sqrt{2\left(\log 2|\Xi| - \log\delta\right)}}\,\frac{1+\frac{1}{2\sqrt{2Nu}}}{2} - \sqrt{\frac{N}{32V}} + \frac{1}{2}. \tag{47}$$

Proof: See Appendix C. ■

Recall that the value of V depends on the quantities u, K and M. When u is reasonably large such that $1-u \ge \frac{M-K}{(M-1)K}$, we have $V = \frac{M-K}{(M-1)K}uN$. When there is no noise in radar returns, a number of scattering points (on the grid) in the scale of $S = O(\sqrt{\frac{KuN}{\log MN}})$ guarantees a unique reconstruction of range-Doppler parameters with high probability according to Theorems 2 and 7. Note that this rather simple asymptotic condition assumes that $\frac{M-1}{M-K} \approx 1$, i.e., that the overall number of available frequencies M is substantially larger than the number of frequencies utilized in each pulse K, thus ensuring the agile character in frequency domain. Compared to the asymptotic condition $O(\sqrt{\frac{N}{\log MN}})$ of FAR with full observations [7], we find that the presence of corrupted observations, i.e. when $u < 1$, leads to degraded range-Doppler reconstruction performance. However, by increasing the number of transmitted frequencies in each pulse K while maintaining $K \ll M$, the performance deterioration due to missing observations can be mitigated, enhancing the interference immunity of the radar in extreme electromagnetic environments. In the special case that $K = 1$ and $u = 1$, i.e., FAR in an interference free environment, the two conditions coincide as $O(\sqrt{\frac{KuN}{\log MN}}) = O(\sqrt{\frac{N}{\log MN}})$.

The above condition is proposed for the noiseless case, indicating that the inherent target/clutter reconstruction capacity increases with $\sqrt{K}$. In practical noisy cases, the reconstruction performance does not monotonically increase with K, because the transmit power of each frequency decreases with K, thus degrading the SNR in both CAESAR and WMAR. Particularly, in CAESAR, larger K means that less antennas (L/K) are allocated to each frequency, which affects the radiation beam and enlarges the gain loss. In addition, a small K maintains the practical advantages of frequency agility in terms of, e.g., ECCM and EMC performance.

VII. SIMULATION RESULTS

In this section, we numerically compare the performance of WMAR, CAESAR, and FAR in noiseless/noisy, clutter, and/or jamming environments. The performance is evaluated in terms of target detection probability, accuracy and resolution, probability of correct reconstruction, and mutual interference, as presented in Subsection VII-A–VII-D, respectively.

We consider a frequency band starting from $f_c = 9$ GHz, with $M = 4$ available carriers and carrier spacing of $\Delta f = 1$ MHz. The radar system is equipped with an antenna array of $L = 10$ elements with spacing of $d = \frac{c}{2f_c}$, and utilizes $N = 32$ pulses focusing on $\theta = 0$. CAESAR and WMAR use $K = 2$ frequencies at each pulse. In noisy scenarios, we use the term SNR for the post-accumulation SNR of WMAR/FAR, i.e., $NL^3|\beta|^2/\sigma^2$ as derived in Subsection V-A. To guarantee fair comparison, we use the same definition for all the radar schemes. In the presence of jamming, we test the pulse selective missing pattern. In order to implement target recovery via Algorithm 1 for the three radar schemes, we use the convex optimization toolbox [28] to implement basis pursuit (29) in noiseless cases or the Lasso algorithm (31) with $\lambda = 0.5$ in noisy setups for range-Doppler reconstruction.

A. Target Detection in Clutter Environment

We compare the detection performance of the proposed WMAR and CAESAR schemes with FAR and conventional fixed frequency radars, which can be regarded as a special case of WMAR, CAESAR and FAR, with $K = 1$ and $\Omega_{n,k} = f_n = f_c$.

The motivation for comparing our schemes to fixed frequency radar here stems from its high clutter rejection capabilities, making its performance a benchmark when studying target detection in the presence of clutter. We evaluate the detection probabilities, P_d, of a moving target under ground clutter environment. The ground clutter is modeled as radar returns from many static scattering points with velocity being zero. Thus, moving targets and ground clutter are distinguishable by observing their Doppler values. We denote by $\mathcal{C}$ the index set corresponding to zero Doppler, i.e., $\mathcal{C} = \{n + mN | n = 0, m \in \mathcal{M}\}$, and by $\mathcal{C}^c$ its complementary set, i.e., $\mathcal{C}^c = \{n + mN | n \in \mathcal{N} \backslash \{0\}, m \in \mathcal{M}\}$. The number of target scattering points is $S_t = 1$. The normalized range and Doppler parameter of the target is determined by randomly selecting the index i from $\mathcal{C}^c$. The target intensity $|\beta_i|, i \in \mathcal{C}^c$ is selected to match the desired SNR. We use the Swerling I model to characterize the clutter [29, Ch. 3], where the clutter is assumed to contain a large number of scatterers and reflection intensity of each scatterer is considered constant during the CPI. The number of clutter scattering points is set as $S_c = 1000$, and the intensity of each scattering point is unity, with a random phase uniformly distributed over $[0, 2\pi)$. The normalized range parameters $\tilde{r}_c$ of these scatterers are uniformly distributed over $[0, 2\pi)$, and are not assumed to lie on the predefined grid points. Since these scatterers have identical velocity, the superposition of their echoes, i.e., the clutter signal, can be represented by radar returns from the grid points indexed by $\mathcal{C}$. Echoes from both target and clutter are treated as unknown, and are reconstructed simultaneously by CS. Particularly, we apply Lasso (31) for range-Doppler reconstruction, yielding $\hat{\boldsymbol{\beta}}$, where elements indexed in $\mathcal{C}$ are regarded as equivalent clutter intensities and the remaining elements are regarded as intensities of moving targets. The P_d curves are plotted versus SNR, and we choose $\sigma^2 = 1$. Similarly with the definition of SNR presented in Subsection V-A, we calculate the clutter to noise ratio after coherent accumulation, which are approximately $S_c N L^3 |\beta_c|^2 / \sigma^2$ for FAR and WMAR, and $S_c N L^3 |\beta_c|^2 / (K^2 \sigma^2)$ for CAESAR, i.e., 75 dB and 69 dB, respectively.

The simulations are carried out in two parts. In the first part, there are only clutter and additive noises in the radar returns, without returns from moving targets. The resulting radar measurements are used to determine the detection thresholds for all radar schemes, respectively, under a given probability of false alarm, denoted P_{fa}. In the second part, these thresholds are used to detect the existence of a target from the received echoes, which now include noise as well as returns from both clutter and moving target. The target detection procedure is based on the estimated parameters $|\hat{\boldsymbol{\beta}}|$, as detailed in Subsection IV-B. In the first part, we set $P_{fa} = 10^{-3}$ and perform 10^5 Monte Carlo trials. While radar systems typically operate at lower values of P_{fa}, we use this value for computational reasons. It can be faithfully simulated under the given number of trials, and the selected value of P_{fa} provides a characterization and understanding of the behavior of the considered radar schemes. A false alarm is proclaimed if any nonzero-Doppler element in $|\hat{\boldsymbol{\beta}}|$ exceeds certain threshold T_h, i.e., $\max_{i \in \mathcal{C}^c} |\hat{\beta}_i| > T_h$. In the second part, we execute 200 Monte Carlo trials. A successful detection is proclaimed if the estimated intensity of the moving target is larger than the threshold, $|\hat{\beta}_i| > T_h, i \in \mathcal{C}^c$. To evaluate the influence of missing observation caused by jamming, we set the survival rate $u = 0.7$ and compare the resulting probability of detection, P_d curves with those of the full observation cases in Fig. 2. Note that the detection thresholds for these P_d curves are calculated individually.

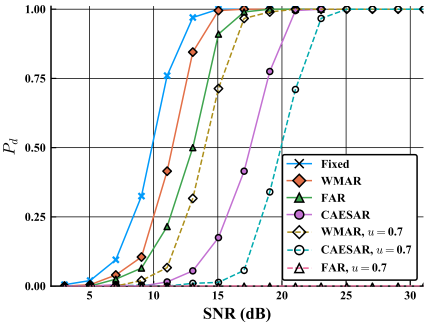

Fig. 2. Detection probabilities P_d versus SNR. The label "Fixed" represents the fixed frequency radar, and the P_d of FAR with $u = 0.7$ are zeros in the tested scenarios.

As shown in Fig. 2, the fixed frequency radar has higher detection probabilities than the counterparts of frequency agile schemes. The advantage of fixed frequency radar stems from the property of its observation matrix $\boldsymbol{\Phi} \in \mathbb{C}^{KN \times MN}$, where $K = M = 1$ and $\boldsymbol{\Phi}$ becomes an orthogonal matrix, benefiting the Doppler reconstruction performance of CS methods. While in the frequency agile schemes, generally it holds that $M > K$, resulting in an incomplete observation matrix and degradation of clutter/target recovery performance. However, the fixed frequency radar is vulnerable to jamming. In the full observation cases, WMAR outperforms FAR because of the increased number of observations. Though CAESAR has identical number of observations with WMAR after receive beamforming, the P_d values of CAESAR are less than those achieved by WMAR with a SNR gap of approximately 6 dB. This follows since CAESAR suffers from an antenna gain loss of K^2 as discussed in Subsection V-A (i.e., 6 dB since $K = 2$). When some of the observations are missing due to jamming, the detection probabilities are affected. Both WMAR and CAESAR suffer from an SNR loss of approximately 3 dB, while FAR fails to detect any moving target in the scenarios under test. When FAR is lacking in radar observations, the mutual coherence property of its observation matrix $\boldsymbol{\Phi}_*$ becomes degraded, leading to many spurious peaks of high intensities in the recovery results $|\hat{\boldsymbol{\beta}}|$. These spurious peaks significantly increase the detection threshold, thus operating under a fixed P_{fa} of 10^{-3} results in notably reduced detection probability P_d.

To summarize, we find from the simulation results that 1) the proposed multi-tones schemes (WMAR and CAESAR) enhance the immunity against missing data over the single-tone FAR, and 2) WMAR outperforms CAESAR due to its higher antenna gain, which comes at the cost of increased instantaneous bandwidth.

B. *Accuracy and Resolution*

Here, we compare the range, Doppler and angle estimate results under different range-Doppler grid points. To this aim, two sets of range-Doppler grid points are tested: one uses the standard grid as mentioned in Subsection IV-B, where the intervals of consecutive range and Doppler grid points are $\Delta_{\tilde{r}} = \frac{2\pi}{M}$ and $\Delta_{\tilde{v}} = \frac{2\pi}{N}$, respectively; The latter uses a denser grid, setting $\Delta_{\tilde{r}} = \frac{2\pi}{2M}$ and $\Delta_{\tilde{v}} = \frac{2\pi}{2N}$, and the consequent

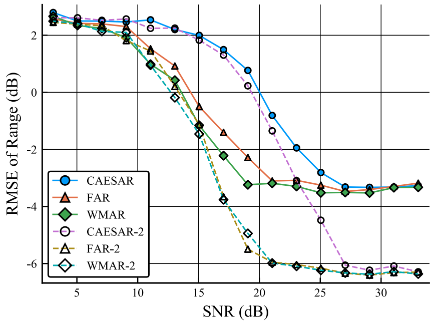

Fig. 3. Range accuracy of range-Doppler reconstruction results.

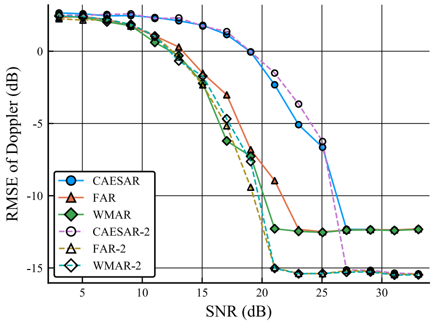

Fig. 4. Doppler accuracy of range-Doppler reconstruction results.

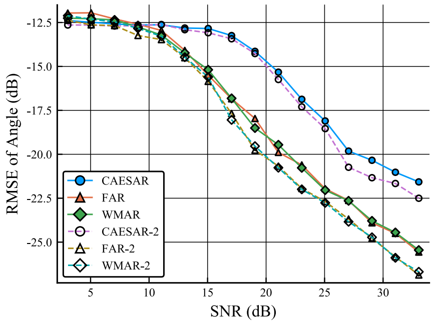

Fig. 5. Angle accuracy versus SNR.

simulation results are denoted with label "-2," e.g., CAESAR-2. The number of scattering points is $S = 1$ without clutter. The normalized range-Doppler parameter, $(\tilde{r}, \tilde{v})$, of the scattering point is uniformly, randomly set over $[0, 2\pi)^2$, and the angle is randomly set within the beam $\vartheta \in \vartheta$. Under this setting, the ground truth of the range-Doppler parameter may be off the grid, which leads to inevitable estimation error. The CS method applied for range-Doppler reconstruction is based on (31), and we estimate range-Doppler, denoted by $(\hat{\tilde{r}}, \hat{\tilde{v}})$, from the index of the element with maximum magnitude in $\hat{\boldsymbol{\beta}}$. We then use root mean squared error (RMSE) as the metric of accuracy, defined by $\sqrt{\mathrm{E}[(\tilde{r} - \hat{\tilde{r}})^2]}$, taking normalized range as an example. The remaining settings are the same as those used in Subsection VII-A. We run 500 Monte Carlo trials and the range, Doppler and angle accuracy results are shown in Figs. 3, 4 and 5, respectively.

As expected, the RMSEs become lower when we increase SNR, while we observe in Figs. 3 and 4 that the RMSEs of range and Doppler estimates reach error floors as the SNR increases. The error floors depend on the grid intervals $\Delta_{\tilde{r}}$ or $\Delta_{\tilde{v}}$, and denser grid points lead to lower error floors. The results also reveal that WMAR and FAR have similar accuracy performance, while CAESAR has an SNR loss of 6 dB in moderate SNR levels because of its lower antenna gain. In high SNR scenarios, the RMSEs of CAESAR also reach the error floor.

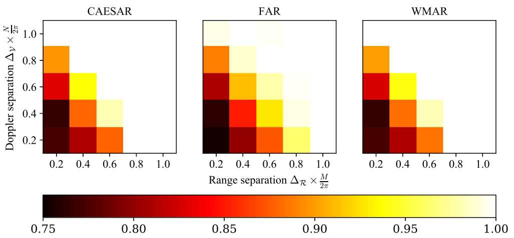

Fig. 6. Hit rates of separating closely spaced scattering points.

We next examine the ability of CAESAR, FAR and WMAR in separating closely spaced scattering points, i.e., obtainable resolution. In the simulations, we use dense grid points with intervals $\Delta_{\tilde{r}} = \frac{2\pi}{5M}$ and $\Delta_{\tilde{v}} = \frac{2\pi}{5N}$. We consider two closely spaced scattering points, of which angles are set $\vartheta = 0$ and range-Doppler parameters are on the grid. Particularly, we fix the range-Doppler parameter of one scattering point $(\tilde{r}_1, \tilde{v}_1) = (0, 0)$ and change the counterpart of the other scattering from $[\Delta_{\tilde{r}}, \frac{2\pi}{M}] \times [\Delta_{\tilde{v}}, \frac{2\pi}{N}]$, such that the range/Doppler separation $(\Delta_{\mathcal{R}}/\Delta_{\mathcal{V}})$ between two points are changed. In this experiment, we disregard noise and the scattering intensities are both $|\beta_1| = |\beta_2| = 1$ with random phase. We use (29) for range-Doppler recovery, and the two most dominant elements in the estimate $\hat{\boldsymbol{\beta}}$ are regarded as scattering points. The indices of these two elements are compared with the corresponding ground truth, and a successful recovery (also referred to a hit) is proclaimed if both indices are correct. The number of Monte Carlo trails are 500. The achievable hit rate results versus separation between scattering points are shown in Fig. 6. The results demonstrate that all the frequency agile schemes, CAESAR, FAR and WMAR have close performance in resolution, while the hit rates of CAESAR and WMAR are slightly higher than those of FAR, because they have more observations and the measurement matrix $\boldsymbol{\Phi}$ has better coherence property.

C. *Reconstruction of Multiple Scattering Points*

In this subsection, we evaluate the proposed radar schemes in recovering a set of S scattering points in noiseless and noisy setups. In both scenarios, we use the standard grid points with grid intervals $(\Delta_{\tilde{r}}, \Delta_{\tilde{v}}) = (2\pi/M, 2\pi/N)$. The range-Doppler parameters of scattering points are randomly selected from the grid points, angle parameters are randomly set from the continuous set ϑ, and scattering intensities are all set to unity. We apply CS methods for range-Doppler recovery, and the indices of S most significant entries in $\hat{\boldsymbol{\beta}}$ are regarded as elements of the estimated support set. Hit rates are applied as performance metric, and a hit is proclaimed if the obtained support set is identical to the ground truth, which means all the range-Doppler parameters are reconstructed correctly.

In the noiseless experiment, we simulate different numbers of recoverable scattering points, S. We set the survival rate $u = 0.4$ for jamming environments. The resulting hit rates versus $S \in \{1, \ldots, N-1\}$ are depicted in Fig. 7. As expected, the hit

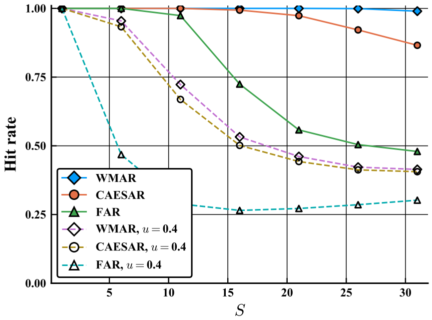

Fig. 7. Range-Doppler recovery versus S, noiseless setting.

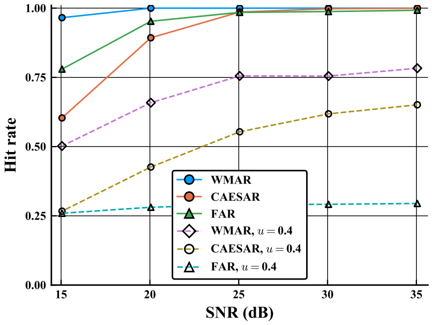

Fig. 8. Range-Doppler recovery versus SNR.

rates decrease as S increases. The performance of CAESAR is within a very small gap of that achievable using WMAR, because CAESAR and WMAR use the same amount of transmitted frequencies K, and the number of beamformed measurements is also the same. Hit rates of CAESAR and WMAR exceed that of FAR significantly. This gain stems from the fact that transmitting multi-carriers in each pulse of CAESAR and WMAR increases the number of observations, and thus raises the number of recoverable scattering points.

We then consider the noisy case, and compare the range-Doppler recovery performance versus SNR, which is changed by varying σ^2. We set $S=10$, and we let $u=0.4$ for the jamming environment. The hit rates of the range-Doppler parameters are depicted in Fig. 8.

Observing Fig. 8, we note that, as expected, WMAR achieves the best performance in range-Doppler reconstruction. While WMAR and CAESAR have the same number of observations, CAESAR has a lower antenna gain as noted in Subsection V-A, which results in its degraded performance compared to WMAR. In the full observation case with high SNRs, i.e., SNR ≥ 25 dB, CAESAR has higher hit rates than FAR due to the advantage of increased number of transmitted frequencies, while in low SNRs of less than 20 dB, FAR exceeds CAESAR owing to its higher antenna gain. In the jamming scenario, CAESAR outperforms FAR, and that FAR almost fails to reconstruct scattering points (with hit rates around 0.25). The superiority of WMAR/CAESAR over FAR demonstrates the advantage of the proposed multi-carrier waveforms.

From the experimental results in Subsection VII-A–VII-C, we find that the multi-carrier signals used by CAESAR and WMAR significantly enhance range-Doppler reconstruction performance over the monotone waveform in FAR. The advantage becomes more distinct in jamming environments, where some radar measurements are invalid. In reasonably high SNR scenarios, the reconstruction performance of CAESAR, which uses narrowband constant modulus waveforms for each antenna element, approach those of WMAR, which uses instantaneously wideband waveforms.

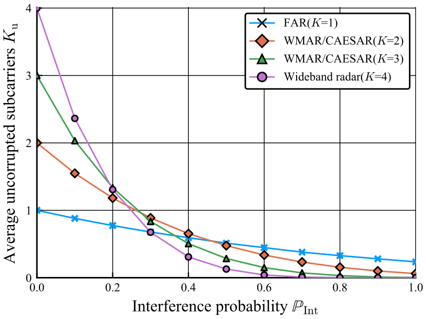

Fig. 9. The average number of uncorrupted subcarriers K_{u} versus $\mathbb{P}_{\mathrm{Int}}$ for radar schemes with different number of transmit subcarriers, which varies from $K=1$ to $K=4$.

D. Mutual Interference

One of the main advantages of frequency agile transmission is its relatively low level of mutual interference, which implies that multiple transmitters can coexist in dense environments. To demonstrate this property of the proposed radar schemes, which all utilize some level of frequency agility, we next evaluate the unintended mutual interference of closely placed radars transmitting the same waveform pattern. We compare the frequency agile schemes of FAR, WMAR and CAESAR, with an instantaneous wideband radar which transmits all subbands simultaneously. In the simulation, we consider a scenario with 6 radars operating independently. Mutual interference occurs if a reference radar is receiving echoes while another radar is transmitting at the same subcarriers with their antenna beams directed towards each other. In this case the echoes of the reference radar at the conflicted subcarriers are corrupted. The level of mutual interference is measured by the average number of uncorrupted subcarriers, denoted K_{u}.

We use $\mathbb{P}_{\mathrm{Int}}$ to represent the probability that one radar may interfere the reference radar, i.e., that it is radiating during the reception period of the reference radar and their beams are directed towards each other. The number of subcarriers transmitted in each pulse varies from $K=1$ to $K=4$, where $K=1$ represents the FAR while $K=4$ represents the radar using full bandwidth. As WMAR and CAESAR transmit the same number of subcarriers for a specific K, their performance on mutual interference is the same. To demonstrate the mutual interference intensity versus interference probabilities, we simulate 10^6 Monte Carlo trials for each interference probability and calculate the average number of uncorrupted subcarriers as shown in Fig. 9. From the results, we observe that, as expected, when the interference probability is small, e.g., less than 0.2, radar systems transmitting more subcarriers are capable of effectively utilizing their bandwidth reliably. However, as the probability of interference grows, wideband radar induce severe mutual interference, resulting in a negligible average number of uncorrupted subcarriers for $\mathbb{P}_{\rm Int} > 0.6$. The frequency agile schemes, such as FAR and WMAR/CAESAR operating with $K = 2$, are still capable of reliably utilizing a notable portion of their bandwidth in the presence of such high interference. These results indicate that the less frequency agile the scheme is, the severer the mutual interference becomes in the high interference probability regime.

VIII. CONCLUSION

In this work we developed two multi-carrier frequency agile schemes for phase array radars: WMAR, which uses wideband waveforms; and CAESAR, which transmits monontone signals and introduces spatial agility. We modeled the received radar signal, and proposed an algorithm for target recovery. We then characterized theoretical recovery guarantees. Our numerical results demonstrate that our proposed schemes achieve enhanced range-Doppler reconstruction performance in the presence of missing pulses, representing extreme electromagnetic environments. Furthermore, it is shown that CAESAR is capable of achieving performance which approaches that of wideband radar, while utilizing narrowband transceivers. An additional benefit which follows from the introduction of frequency and spatial agility is the natural implementation of CAESAR as a DFRC system, studied in a companion paper.

APPENDIX

A. *proof of Lemma 1*

In the following we prove (23) for CAESAR. The proof for WMAR follows similar arguments and is omitted for brevity.

Substituting the definitions of $\boldsymbol{w}, \boldsymbol{P}$ and $\boldsymbol{Y}$ into (22) yields

$$\begin{aligned} Z_{k,n} =& \sum_{l=0}^{L-1} w_l\left(\theta, \Omega_{n,k}\right)\left[\boldsymbol{p}(n,k)\right]_l \sum_{s=0}^{S-1} \tilde{\beta}_s e^{j\tilde{r}_s c_{n,k}} \\ & e^{j\tilde{v}_s n\zeta_{n,k}} e^{-j2\pi\Omega_{n,k} ld \sin\vartheta_s/c} \rho_{\rm C}(n,k,\delta_{\vartheta_s}) \\ =& \sum_{s=0}^{S-1}\sum_{l=0}^{L-1} \left[\boldsymbol{p}(n,k)\right]_l \tilde{\beta}_s e^{j\tilde{r}_s c_{n,k}} e^{j\tilde{v}_s n\zeta_{n,k}} \\ & e^{-j2\pi\Omega_{n,k} ld(\sin\vartheta_s - \sin\theta)/c} \rho_{\rm C}(n,k,\delta_{\vartheta_s}) \\ =& \sum_{s=0}^{S-1} \tilde{\beta}_s e^{j\tilde{r}_s c_{n,k}} e^{j\tilde{v}_s n\zeta_{n,k}} \rho_{\rm C}^2(n,k,\delta_{\vartheta_s}). \end{aligned} \tag{A.1}$$

Recall that when $\delta_{\vartheta_s} \approx 0$ it holds that $\rho_{\rm C}(n,k,\delta_{\vartheta_s}) \approx L/K = \sqrt{\alpha_K}$. Then, (A.1) reduces to (23), proving the lemma.

B. *proof of Lemma 4*

We first prove (44) and (45), after which we address (46).

1) *Proof of (44) and (45):* For brevity, let $p = -\Delta_m$, $q = -\Delta_n$, $I_n = I_\Lambda(n)$, and $B = \binom{M}{K}$. We set $\binom{M}{K} = 0$ when $M \leq 0$ or $K < 0$, and $\binom{M}{0} = 1$ when $M > 0$.

We first compute $\mathrm{E}[\chi_n] = \frac{1}{K}\mathrm{E}[I_n e^{jqn}\sum_{k=0}^{K-1} e^{jpc_{n,k}}]$. The expectation is taken over the indicator I_n and frequency codes $c_{n,k}$. Since they are independent and $\mathrm{E}[I_n] = u$, it holds that

$$\mathrm{E}\left[\chi_n\right] = \frac{ue^{jqn}}{K}\mathrm{E}\left[\sum_{k=0}^{K-1} e^{jpc_{n,k}}\right]. \tag{B.1}$$

Since K frequencies are selected uniformly (but not independently), it follows that

$$\mathrm{E}\left[\sum_{k=0}^{K-1} e^{jpc_{n,k}}\right] = \frac{1}{B}\sum_{i=0}^{B-1}\sum_{k=0}^{K-1} e^{jpm_{i,k}}, \tag{B.2}$$

where $m_{i,k}$ denotes the k-th frequency in the i-th combination. Out of these B combinations, there are $\binom{M-1}{K-1}$ that contain a given selection $m \in \mathcal{M}$. Thus, we have that

$$\sum_{i=0}^{B-1}\sum_{k=0}^{K-1} e^{jpm_{i,k}} = \binom{M-1}{K-1}\sum_{m=0}^{M-1} e^{jpm} = \frac{BK}{M}\sum_{m=0}^{M-1} e^{jpm}. \tag{B.3}$$

Substituting (B.3) into (B.2) yields

$$\mathrm{E}\left[\sum_{k=0}^{K-1} e^{jpc_{n,k}}\right] = \frac{K}{M}\sum_{m=0}^{M-1} e^{jpm} = \frac{K}{M}\frac{1-e^{jpM}}{1-e^{jp}}. \tag{B.4}$$

As $p \in \{\frac{2\pi m}{M}\}_{m\in\mathcal{M}}$, it holds that $\mathrm{E}[\sum_{k=0}^{K-1} e^{jpc_{n,k}}] = K$ if $p = 0$ and zero otherwise. Substituting this into (A.2), we have

$$\mathrm{E}\left[\chi_n\right] = \begin{cases} ue^{jqn}, & \text{if } p = 0, \\ 0, & \text{otherwise}, \end{cases} \tag{B.5}$$

which proves (44).

To obtain $\mathrm{D}[\chi_n] := \mathrm{E}[|\chi_n - \mathrm{E}[\chi_n]|^2]$, we consider two cases, $p = 0$ and $p \neq 0$. When $p = 0$, we have $\chi_n = I_n e^{jqn}$ and

$$\begin{aligned} \mathrm{E}\left[\left|I_n e^{jqn} - ue^{jqn}\right|^2\right] &= \mathrm{E}\left[\left(I_n - u\right)^2\right] \\ &\overset{(a)}{=} \mathrm{E}\left[I_n + u^2 - 2I_n u\right] \overset{(b)}{=} u - u^2, \end{aligned} \tag{B.6}$$

where (a) holds since $I_n^2 = I_n$ and in (b) we apply $\mathrm{E}[I_n] = u$.

When $p \neq 0$, the random variable χ_n has zero mean, and its variance is given by

$$\begin{aligned} \mathrm{E}\left[\left|\chi_n\right|^2\right] &= \mathrm{E}\left[\frac{I_n}{K}\left|\sum_{k=0}^{K-1} e^{jpc_{n,k}+jqn}\right|^2\right] \\ &= \frac{1}{K^2}\mathrm{E}\left[I_n \cdot \sum_{k=0}^{K-1}\sum_{k'=0}^{K-1} e^{jp\left(c_{n,k}-c_{n,k'}\right)}\right] \\ &= \frac{u}{K^2}\mathrm{E}\left[\sum_{k=0}^{K-1}\sum_{k'=0}^{K-1} e^{jp\left(c_{n,k}-c_{n,k'}\right)}\right], \end{aligned} \tag{B.7}$$

where we use $I_n^2 = I_n$. To compute (A.8), we note that

$$\begin{aligned} &\mathrm{E}\left[\sum_{k=0}^{K-1}\sum_{k'=0}^{K-1} e^{jpc_{n,k}-jpc_{n,k'}}\right] \\ &= \frac{\binom{M-1}{K-1}}{B}\sum_{m=0}^{M-1} e^{jp\cdot 0} + \frac{\binom{M-2}{K-2}}{B}\sum_{m=0}^{M-1}\sum_{\substack{m'=0,\\ m'\neq m}}^{M-1} e^{jp(m-m')} \\ &\overset{(a)}{=} \frac{\binom{M-1}{K-1} - \binom{M-2}{K-2}}{B}M + \frac{\binom{M-2}{K-2}}{B}\sum_{m=0}^{M-1}\sum_{m'=0}^{M-1} e^{jp(m-m')}, \end{aligned} \tag{B.8}$$

where (a) follows since $\sum_{m=0}^{M-1}\sum_{m'=0,m'\neq m}^{M-1} e^{jp(m-m')}$ in the second term can be replaced by $\sum_{m=0}^{M-1}\sum_{m'=0}^{M-1} e^{jp(m-m')} - \sum_{m=0}^{M-1} e^{0}$. From the derivation of (A.6), it holds that for $p \neq 0$ the second summand in (A.9) vanishes, resulting in

$$\mathrm{E}\left[\sum_{k=0}^{K-1}\sum_{k'=0}^{K-1} e^{jpc_{n,k}-jpc_{n,k'}}\right] = \frac{(M-K)K}{M-1}. \tag{B.9}$$

Plugging (B.9) into (B.7), we obtain

$$\mathrm{E}\left[|\chi_n|^2\right] = \frac{M-K}{(M-1)K}u, \text{ if } p \neq 0. \tag{B.10}$$

Finally, to prove (45), we calculate $\sum_{n=0}^{N-1}\mathrm{D}[\chi_n]$ for $p=0$ and $p \neq 0$. When $p=0$, from (A.7), we have that

$$\sum_{n=0}^{N-1}\mathrm{D}\left[\chi_n\right] = \sum_{n=0}^{N-1}\left(u-u^2\right) = \left(u-u^2\right)N. \tag{B.11}$$

When $p \neq 0$, it follows from (B.10) that $\sum_{n=0}^{N-1}\mathrm{D}[\chi_n] = \frac{M-K}{(M-1)K}uN$. Combining this and (B.11) proves (45).

2) proof of (46) We again consider the two cases $p=0$ and $p \neq 0$ separately: When $p=0$, it follows from (A.6) that

$$\begin{aligned}\left|\chi_n - \mathrm{E}\left[\chi_n\right]\right|^2 &= \left|\left(I_n-u\right)e^{jqn}\right|^2 = \left(I_n-u\right)^2\\ &= \begin{cases}(1-u)^2 \leq 1, & \text{if } I_n = 1,\\ u^2 \leq 1, & \text{otherwise.}\end{cases}\end{aligned} \tag{B.12}$$

When $p \neq 0$, $|\chi_n - \mathrm{E}[\chi_n]|^2 = |\chi_n|^2$, which is not larger than 1 by definition of χ_n (42), thus proving (46).

C. proof of Theorem 7

By fixing some positive $\epsilon \leq V$, setting $t = \sqrt{\frac{N}{8V}}\epsilon$ and

$$\epsilon' := \frac{\sqrt{V}+\epsilon}{uN - \sqrt{\frac{N}{8V}}\epsilon} = \frac{\sqrt{V}+\epsilon}{uN-t}, \tag{C.1}$$

we have that for any $(\Delta_m, \Delta_n) \in \Xi$

$$\begin{aligned}\mathbb{P}\left(\frac{|\chi|}{|\Lambda|} \geq \epsilon'\right) &\overset{(a)}{\leq} \mathbb{P}\left(|\chi| \geq \sqrt{V}+\epsilon \cup |\Lambda| \leq uN-t\right)\\ &\leq \mathbb{P}\left(|\chi| \geq \sqrt{V}+\epsilon\right) + \mathbb{P}\left(|\Lambda| \leq uN-t\right)\\ &\overset{(b)}{\leq} 2e^{-\frac{\epsilon^2}{4V}}.\end{aligned} \tag{C.2}$$

Here (a) holds since the event $\frac{|\chi|}{|\Lambda|} \geq \frac{\sqrt{V}+\epsilon}{uN-t}$ implies that at least one of the conditions $|\chi| \geq \sqrt{V}+\epsilon$ and $|\Lambda| \leq uN-t$ is satisfied; and (b) follows from Corollary 5 and Lemma 6.

Using the bound (C.2) on the magnitude of the normalized correlation, we next bound the probability of $\mu(\mathbf{\Phi}_*)$ to exceed some constant. By applying the union bound to (43), we have

$$\begin{aligned}\mathbb{P}\left(\mu(\mathbf{\Phi}_*) \geq \epsilon'\right) &\leq \sum_{(\Delta_m,\Delta_n)\in\Xi} \mathbb{P}\left(\frac{\left|\chi\left(\Delta_m,\Delta_n\right)\right|}{|\Lambda|} > \epsilon'\right)\\ &\leq 2|\Xi|e^{-\frac{\epsilon^2}{4V}}.\end{aligned} \tag{C.3}$$

According to (C.3), for any $\epsilon > 0$, it holds that

$$\mathbb{P}\left(\mu(\mathbf{\Phi}_*) \leq \epsilon'\right) \geq 1 - 2|\Xi|e^{-\frac{\epsilon^2}{4V}}, \tag{C.4}$$

where ϵ' is obtained from ϵ via (C.1). The right hand side of (C.4) is not smaller than $1-\delta$ when $\delta \geq 2|\Xi|e^{-\frac{\epsilon^2}{4V}}$, implying that $\mathbb{P}(\mu(\mathbf{\Phi}_*) \leq \epsilon') \geq 1-\delta$ when ϵ satisfies

$$\epsilon \geq \sqrt{2V(\log 2|\Xi| - \log\delta)}. \tag{C.5}$$

Finally, by (C.1), fixing $\epsilon' = 1/(2S-1)$ implies that

$$S = \frac{uN - \sqrt{\frac{N}{8V}}\epsilon}{2\sqrt{V}+2\epsilon} + \frac{1}{2} = \frac{uN + \sqrt{N/8}}{2\sqrt{V}+2\epsilon} - \sqrt{\frac{N}{32V}} + \frac{1}{2}. \tag{C.6}$$

Substituting (C.5) into (C.6) proves (47).

REFERENCES

[1] T. Huang, Y. Liu, Y. C. Eldar, and X. Wang, "Multiple carrier agile radar via compressed sensing," in *Proc. Int. Workshop Compressed Sens. Appl. Radar, Multimodal Sens., Imag.*, 2018.

[2] T. Huang, Y. Liu, D. Ma, N. Shlezinger, and Y. C. Eldar, "Multi-carrier agile phased array radar," in *Proc. IEEE Int. Conf. Signal, Inf. Data Process.*, 2019, pp. 1–6.

[3] T. Huang, N. Shlezinger, X. Xu, D. Ma, Y. Liu, and Y. C. Eldar, "Theoretical analysis of multi-carrier agile phased array radar," in *Proc. IEEE Int. Conf. Acoust., Speech, Signal Process.*, 2020, pp. 4702–4706.

[4] S. R. J. Axelsson, "Analysis of random step frequency radar and comparison with experiments," *IEEE Trans. Geosci. Remote Sens.*, vol. 45, no. 4, pp. 890–904, Apr. 2007.

[5] J. Yang, J. Thompson, X. Huang, T. Jin, and Z. Zhou, "Random-frequency SAR imaging based on compressed sensing," *IEEE Trans. Geosci. Remote Sens.*, vol. 51, no. 2, pp. 983–994, Feb. 2013.

[6] D. Cohen, K. V. Mishra, and Y. C. Eldar, "Spectrum sharing radar: Coexistence via Xampling," *IEEE Trans. Aerosp. Electron. Syst.*, vol. 54, no. 3, pp. 1279–1296, Jun. 2018.

[7] T. Huang, Y. Liu, X. Xu, Y. C. Eldar, and X. Wang, "Analysis of frequency agile radar via compressed sensing," *IEEE Trans. Signal Process.*, vol. 66, no. 23, pp. 6228–6240, Dec. 2018.

[8] W. Rao, G. Li, X. Wang, and X. Xia, "ISAR imaging of maneuvering targets with missing data via matching pursuit," in *Proc. IEEE RadarCon*, May 2011, pp. 124–128.

[9] H. Sun, F. Brigui, and M. Lesturgie, "Analysis and comparison of MIMO radar waveforms," in *Proc. IEEE Int. Radar Conf.*, Oct. 2014, pp. 1–6.

[10] D. Cohen, D. Cohen, and Y. C. Eldar, "High resolution FDMA MIMO radar," *IEEE Trans. Aerosp. Electron. Syst.*, vol. 56, no. 4, pp. 2806–2822, Aug. 2020.

[11] D. Cohen, D. Cohen, Y. C. Eldar, and A. M. Haimovich, "SUMMeR: Sub-Nyquist MIMO Radar," *IEEE Trans. Signal Process.*, vol. 66, no. 16, pp. 4315–4330, Aug. 2018.

[12] P. Antonik, M. C. Wicks, H. D. Griffiths, and C. J. Baker, "Frequency diverse array radars," in *Proc. IEEE Conf. Radar*, Apr. 2006.

[13] Y. Liu, H. Ruan, L. Wang, and A. Nehorai, "The random frequency diverse array: A new antenna structure for uncoupled direction-range indication in active sensing," *IEEE J. Sel. Topics Signal Process.*, vol. 11, no. 2, pp. 295–308, Mar. 2017.

[14] E. Brookner, "MIMO radar demystified and where it makes sense to use," in *Proc. IEEE Int. Symp. Phased Array Syst. Technol.*, Oct. 2013, pp. 399–407.

[15] S. Chen and F. Xi, "Quadrature compressive sampling for multiband radar echo signals," *IEEE Access*, vol. 5, pp. 19 742–19 760, 2017.

[16] D. Ma, N. Shlezinger, T. Huang, Y. Liu, and Y. C. Eldar, "Joint radar-communication strategies for autonomous vehicles: Combining two key automotive technologies," *IEEE Signal Process. Mag.*, vol. 37, no. 4, pp. 85–97, Jul. 2020.

[17] T. Huang, N. Shlezinger, X. Xu, Y. Liu, and Y. C. Eldar, "MAJoRCom: A dual-function radar communication system using index modulation," *IEEE Trans. Signal Process.*, vol. 68, pp. 3423–3438, 2020.

[18] S. U. Pillai, *Array Signal Processing*, in C. S. Burrus, Ed., New York, U.S., Springer-Verlag, 1989, https://www.springer.com/gp/book/9781461281863

[19] M. A. Richards, *Fundamentals Radar Signal Processing*. McGraw-Hill Education, New York, U.S. 2005.

[20] S. R. J. Axelsson, "Suppression of noise floor and dominant reflectors in random noise radar," in *Proc. Int. Radar Symp.*, May 2006, pp. 1–4.

[21] Y. C. Eldar and G. Kutyniok, *Compressed Sensing: Theory and Applications*. Cambridge, U.K.: Cambridge Univ. Press, 2012.

[22] J. Fuchs, "On sparse representations in arbitrary redundant bases," *IEEE Trans. Inf. Theory*, vol. 50, no. 6, pp. 1341–1344, Jun. 2004.

[23] T. T. Cai, L. Wang, and G. Xu, "Stable recovery of sparse signals and an oracle inequality," *IEEE Trans. Inf. Theory*, vol. 56, no. 7, pp. 3516–3522, Jul. 2010.

[24] G. Tang, B. N. Bhaskar, P. Shah, and B. Recht, "Compressed sensing off the grid," *IEEE Trans. Inf. Theory*, vol. 59, no. 11, pp. 7465–7490, Nov. 2013.

[25] D. S. Pham and A. M. Zoubir, "Estimation of multicomponent polynomial phase signals with missing observations," *IEEE Trans. Signal Process.*, vol. 56, no. 4, pp. 1710–1715, Apr. 2008.

[26] D. Gross, "Recovering low-rank matrices from few coefficients in any basis," *IEEE Trans. Inform. Theory*, vol. 57, no. 3, pp. 1548–1566, Mar. 2011.

[27] M. Okamoto, "Some inequalities relating to the partial sum of binomial probabilities," *Ann. Inst. Statist. Math.*, vol. 10, no. 1, pp. 29–35, Mar. 1959.

[28] M. Udell, K. Mohan, D. Zeng, J. Hong, S. Diamond, and S. Boyd, "2014 First Workshop for High Performance Technical Computing in Dynamic Languages," in *Convex Opt. Julia*, pp. 18–28, 2014.

[29] M. Budge and S. German, *Basic Radar Analysis*, ser. Artech House radar series. Artech House, Boston, U.S. 2015.

Tianyao Huang received the B.S. degree in telecommunication engineering from the Harbin Institute of Technology, Harbin, China, in 2009, and the Ph.D. degree in electronics engineering from Tsinghua University, Beijing, China, in 2014. From 2014 to 2017, he was a Radar Researcher with Aviation Industry Corporation of China (AVIC). Since July 2017, he has joined Intelligent Sensing Lab, Department of Electronic Engineering, Tsinghua University, as an Assistant Professor. His current research interests include signal processing, compressed sensing, and joint radar communications system design.

Nir Shlezinger (Member, IEEE) received the B.Sc., M.Sc., and Ph.D. degrees from Ben-Gurion University, Beersheba, Israel, in 2011, 2013, and 2017, respectively, all in electrical and computer engineering. From 2017 to 2019, he was a Postdoctoral Researcher with the Technion, Israel Institute of Technology, and from 2019 to 2020, he was a Postdoctoral Researcher with the Signal Acquisition Modeling, Processing, and Learning Lab, Weizmann Institute of Science. He is currently an Assistant Professor with the School of Electrical and Computer Engineering, Ben-Gurion University. From 2009 to 2013, he was a research and development engineer with Yitran Communications. His research interests are in the intersection of communications, signal processing, information theory, and machine learning.

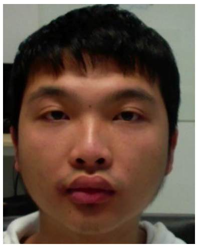

Xingyu Xu received the B.S. degree in 2019 from the Department of Electronic Engineering, Tsinghua University, Beijing, China, where he is currently working toward the Ph.D. His research interests include topological and statistical data analysis.

Dingyou Ma received the B.S. degree in aerospace science and technology from Xidian University, Xi'an, China, in 2016. He is currently working toward the Ph.D. degree with the Department of Electronic Engineering, Tsinghua University, Beijing, China. His research interests are the system design and signal processing on dual-function radar-communications system.

Yimin Liu (Member, IEEE) received the B.S. and Ph.D. degrees (both with Hons.) in electronics engineering from Tsinghua University, Beijing, China, in 2004 and 2009, respectively. From 2004, he was with the Intelligence Sensing Lab (ISL), Department of Electronic Engineering, Tsinghua University. He is currently an Associate Professor with Tsinghua, where his field of activity is study on new concept radar and other microwave sensing technologies. His current research interests include radar theory, statistic signal processing, compressive sensing and their applications in radar, spectrum sensing, and intelligent transportation systems.

Yonina C. Eldar (Fellow, IEEE) received the B.Sc. degree in physics and the B.Sc. degree in electrical engineering from Tel-Aviv University, Tel-Aviv, Israel, 1995 and 1996, respectively, and the Ph.D. degree in electrical engineering and computer science from the Massachusetts Institute of Technology (MIT), Cambridge, MA, USA, in 2002.

She is currently a Professor with the Department of Mathematics and Computer Science, Weizmann Institute of Science, Rehovot, Israel. She was previously a Professor with the Department of Electrical Engineering, Technion, where she held the Edwards Chair in Engineering. She is also a Visiting Professor with MIT, a Visiting Scientist with the Broad Institute, and an Adjunct Professor with Duke University, and was a Visiting Professor with Stanford. She is a member of the Israel Academy of Sciences and Humanities (elected 2017) and a EURASIP Fellow. She is also the author of the book *Sampling Theory: Beyond Bandlimited Systems* and coauthor of four other books published by Cambridge University Press. Her research interests include statistical signal processing, sampling theory and compressed sensing, learning and optimization methods, and their applications to biology, medical imaging and optics.

Dr. Eldar has received many awards for excellence in research and teaching, including the IEEE Signal Processing Society Technical Achievement Award (2013), the IEEE/AESS Fred Nathanson Memorial Radar Award (2014), and the IEEE Kiyo Tomiyasu Award (2016). She was a Horev Fellow of the Leaders in Science and Technology program with the Technion and an Alon Fellow. She received the Michael Bruno Memorial Award from the Rothschild Foundation, the Weizmann Prize for Exact Sciences, the Wolf Foundation Krill Prize for Excellence in Scientific Research, the Henry Taub Prize for Excellence in Research (twice), the Hershel Rich Innovation Award (three times), the Award for Women with Distinguished Contributions, the Andre and Bella Meyer Lectureship, the Career Development Chair with the Technion, the Murieland David Jacknow Award for Excellence in Teaching, and the Technions Award for Excellence in Teaching (two times). She received several best paper awards and best demo awards together with her research students and colleagues including the SIAM outstanding Paper Prize, the UFFC Outstanding Paper Award, the Signal Processing Society Best Paper Award and the IET Circuits, Devices and Systems Premium Award, and was selected as one of the 50 most influential women in Israel and in Asia. She is also a highly cited researcher. She was a member of the Young Israel Academy of Science and Humanities and the Israel Committee for Higher Education. She is the Editor-in-Chief for *Foundations and Trends in Signal Processing*, a member of the IEEE Sensor Array and Multichannel Technical Committee and serves on several other IEEE committees. In the past, she was a Signal Processing Society Distinguished Lecturer, a member of the IEEE Signal Processing Theory and Methods and Bio Imaging Signal Processing technical committees, and served as an Associate Editor for the IEEE TRANSACTIONS ON SIGNAL PROCESSING, *EURASIP Journal of Signal Processing*, *SIAM Journal on Matrix Analysis and Applications*, and *SIAM Journal on Imaging Sciences*. She was the Co-Chair and Technical Co-Chair of several international conferences and workshops.